IGF1 peptide targets Rett Syndrome astrocytes to degrade IGF binding protein, rescue synaptogenesis and restore mitochondrial function

Authors: Prachi Ojha[a], Velina Kozareva[b], Alexandria Barlowe[a], Fabian Schulte[c], Ruby Minh Lam[a], Danielle L Tomasello[d], Ernest Fraenkel[b], Rudolf Jaenisch[d,e], Mriganka Sur[a,f,*]

Affiliations:

a. The Picower Institute for Learning and Memory, Massachusetts Institute of Technology, Cambridge, MA, USA

b. Department of Biological Engineering, Massachusetts Institute of Technology, Cambridge, MA, USA

c. Whitehead Institute for Biomedical Research, Quantitative Proteomics Core, Cambridge, MA, USA

d. Whitehead Institute for Biomedical Research, Cambridge, MA, USA

e. Department of Biology, Massachusetts Institute of Technology, Cambridge, MA, USA

f. Department of Brain and Cognitive Sciences, Massachusetts Institute of Technology, Cambridge, MA, USA

* Corresponding author: msur@mit.edu

Keywords: Astrocyte-neuron interactions, synaptogenesis, proteomics, MeCP2, neurodevelopmental disorders

Abstract

Rett syndrome (RTT), a severe neurodevelopmental disorder caused by mutations in MECP2, leads to profound synaptic and circuit deficits in the brain. While neurons have historically been the focus of RTT pathology, emerging evidence implicates astrocytes in non-cell autonomous mechanisms that impair synaptic structure, function and development. Here, we uncover a central role for astrocyte-secreted IGFBP2 in mediating these deficits and demonstrate that treatment with an IGF1-derived peptide restores synapse formation by promoting IGFBP2 degradation. Using an indirect astrocyte-neuron co-culture system, we show that astrocytes derived from RTT model mice suppress excitatory synapse formation in wild-type neurons and that this impairment is reversed when RTT astrocytes are treated with IGF1(1-3) peptide. Proteomic analysis reveals elevated levels of IGFBP2 in RTT astrocytes and their conditioned media. IGF1(1-3) peptide treatment leads to proteasomal degradation of IGFBP2, increasing IGF1 bioavailability, restoring mitochondrial function, and enhancing downstream PI3K/Akt signaling in neurons. Our data define a molecular mechanism by which astrocyte dysfunction in RTT can be rescued and provide a mechanistic basis for the therapeutic efficacy of IGF1(1-3) peptide, including Trofinetide, an FDA-approved IGF1 peptide mimetic, in RTT.

Significance Statement

Astrocyte dysfunction is increasingly recognized as a contributor to neurodevelopmental disorders, yet precise mechanisms remain elusive. Here, we identify IGFBP2 as a key astrocyte-derived inhibitor of synaptogenesis in Rett syndrome. We show that an IGF1-derived peptide, IGF1(1-3), depletes IGFBP2 via proteasomal degradation. This restores IGF1 bioavailability and rescues synaptic function in a non-cell-autonomous manner. These findings provide a mechanistic explanation for the clinical efficacy of IGF1 peptide and its mimetics in Rett syndrome, and highlight astrocytes as rational therapeutic targets in neurodevelopmental and other disorders.

Introduction

Rett syndrome (RTT) is a severe neurodevelopmental disorder caused by mutations in the X-linked gene *MECP2* (1, 2), encoding methyl-CpG binding protein, which binds to DNA widely across the genome. Originally described as a transcriptional repressor (3, 4), MeCP2 is now recognized to have diverse functions (5, 6), including roles as transcriptional activator as well as repressor (7-9). The loss of MeCP2 thus has pleiotropic effects, making the functional analysis of its downstream pathways essential for devising therapeutic strategies. A pivotal discovery was that RTT is a reversible disorder; restoring MeCP2 expression even after symptom onset can rescue neurological function in mouse models, indicating that underlying synaptic circuits remain immature but plastic and potentially amenable to maturation (10, 11). In studies of activity-dependent cortical plasticity, we identified insulin-like growth factor 1 (IGF1) signaling as a key pathway that promotes synaptic maturation during development: reduced IGF1 signaling accompanies visual deprivation-induced plasticity of neuronal responses and circuits in visual cortex, whereas systemic application of IGF1(1-3), an active tripeptide fragment of IGF1, upregulates IGF1 signaling, promotes synaptic maturation, and prevents such plasticity (12). We subsequently showed that systemic administration of IGF1(1-3), or of full-length IGF1, improves synaptic maturation, spine density, circuit function, and behavior in Mecp2 null mice (13-17). These findings provided the foundation for clinical trials of IGF1 and IGF1 peptide in RTT, including trials with Trofinetide - a mimetic of IGF1(1-3) with an added methyl group making it resistant to breakdown and prolonging its bioavailability - leading to the recent FDA approval of Trofinetide as the first disease-modifying therapeutic for RTT (18, 19). However, the cellular and molecular mechanisms by which IGF1(1-3) peptide or Trofinetide exert their therapeutic effects remain incompletely understood (20).

While RTT was initially considered a neuron-intrinsic disorder, astrocytes are now recognized as critical contributors to disease pathophysiology (21-23). Conditioned medium from MeCP2-deficient astrocytes fails to support synapse formation in wild-type neurons, indicating the presence of astrocyte-derived factors that actively impair synaptic connections and neuronal function through non-cell autonomous mechanisms (24-28). Furthermore, astrocyte conditioned media from mouse models of RTT show upregulation of IGF binding proteins (29), suggesting a mechanism for decreased IGF1 signaling in RTT. Thus, MeCP2 deficiency alters the expression of a range of astrocyte-secreted molecules that influence neurons, and reversing these changes presents a compelling potential target for therapeutic strategies for RTT.

Here, we identify insulin-like growth factor binding protein 2 (IGFBP2) as a major astrocyte-secreted inhibitor of synaptogenesis in RTT. We show that IGFBP2 is upregulated in RTT astrocytes, and that treatment with IGF1(1-3) peptide induces its proteasome-dependent degradation. IGFBP2 binds to and sequesters IGF1, and its degradation restores IGF1 bioavailability, upregulates PI3K/Akt signaling in neurons, and rescues synaptic protein expression. Furthermore, our proteomic profiling reveals a previously unrecognized connection to mitochondrial dysfunction: while IGF1 primarily interacts with mitochondrial proteins in healthy astrocytes, its interactome in RTT astrocytes shifts to proteasomal components. IGF1(1-3) peptide treatment reverses the associated mitochondrial deficits, restoring metabolic support for neurons. Our findings define an astrocyte-centered mechanism for the effectiveness of IGF1(1-3) peptide and Trofinetide, linking IGFBP2 degradation to the restoration of both synaptic signaling and mitochondrial function, and identify this mechanism as a promising therapeutic node for RTT and other neurodevelopmental disorders.

Results

MeCP2-deficient astrocytes impair excitatory synapse formation via non-cell-autonomous mechanisms

To investigate the contribution of astrocytes to Rett syndrome pathogenesis, we established a neuron-astrocyte co-culture system using combinations of primary mouse wild-type and Mecp2$^{tm1.1Bird}$/J knockout astrocytes (WT-A, KO-A) and neurons (WT-N, KO-N) (Fig. 1a). This system allowed us to independently manipulate astrocyte and neuronal genotype and thereby isolate the effects of astrocytes on neuronal synapse formation.

We first examined dendritic spine structure in matched genotype co-cultures. Neurons from KO mice cultured with KO astrocytes exhibited a significant reduction in dendritic spine number and density compared to WT-N + WT-A cultures (Fig. 1b-d), indicating that Rett syndrome model co-cultures display structural synaptic abnormalities. However, because both neurons and astrocytes differ in these conditions, this experiment does not distinguish whether these defects arise from neuronal, astrocytic, or combined contributions.

To characterize astrocytic MeCP2 status in this system, we measured MeCP2 protein expression in cultured astrocytes. WT astrocytes expressed higher levels of MeCP2 compared to heterozygous astrocytes, whereas KO astrocytes lacked detectable MeCP2 expression (SI Appendix, Fig. S1a, b). Astrocyte morphology was also altered in KO-A + KO-N co-cultures (SI Appendix, Fig. S1c, d), consistent with cellular changes accompanying MeCP2 loss.

We next asked whether astrocytes specifically contribute to the observed synaptic abnormalities. To this end, we quantified the colocalization of the excitatory postsynaptic marker PSD-95 with the presynaptic marker Bassoon across all neuron-astrocyte combinations. WT-N cultured with KO-A exhibited a ~50% reduction in PSD-95/Bassoon colocalization compared to WT-N cultured with WT-A controls (33.7 ± 3.2% vs. 64.5 ± 6.2%) (Fig. 1e, f), demonstrating that KO astrocytes are sufficient to impair excitatory synaptogenesis in otherwise wild-type neurons. This impairment was further exacerbated in KO-N + KO-A co-cultures (25.6 ± 4.1%) and was partially rescued when KO neurons were cultured with WT astrocytes (45.4 ± 7.9%) (Fig. 1e, f), indicating that both astrocytic and neuronal MeCP2 contribute to synaptic deficits, with astrocytes exerting a strong non-cell-autonomous effect. Because PSD-95 expression is altered in KO neurons, we also assessed total PSD-95 levels by immunoblotting (SI Appendix, Fig. S1g, h), and therefore expressed synapse measurements as the fraction of PSD-95 puncta colocalized with Bassoon per 50 µm dendritic segment.

In contrast, inhibitory synapse formation, assessed by Gephyrin/Bassoon colocalization, was unchanged across all co-culture conditions (SI Appendix, Fig. S1e, f), indicating that MeCP2 deficiency selectively affects excitatory, but not inhibitory, synaptogenesis.

Together, these results indicate that structural synaptic abnormalities observed in Rett syndrome are accompanied by a selective impairment in excitatory synapse formation driven in part by MeCP2-deficient astrocytes.

IGF1(1-3) peptide treatment of astrocytes restores synapse numbers in neurons

To test whether IGF1(1-3) peptide can rescue synaptic impairments caused by KO-A, we treated astrocytes with the peptide prior to co-culture with neurons (see Methods). Because our previous study only tested the efficacy of this peptide *in vivo* and not in cultures (13), we first performed an *in vitro* dose-response assay to determine the appropriate concentration of the peptide to be used to activate downstream signaling pathways. Specifically, we measured phospho-ERK (p-ERK) levels, which are upregulated upon treatment with full-length IGF1. All three doses of the peptide (50 ng/mL, 100 ng/mL, and 200 ng/mL) were effective in increasing p-ERK levels in KO astrocytes (SI Appendix, Fig. S1i, j). As all doses were effective, we selected the intermediate concentration (100 ng/mL) for all subsequent experiments to minimize potential off-target effects.

We found that WT-N co-cultured with KO-A treated with IGF1 peptide exhibited significantly increased dendritic spine density and synapse numbers compared to untreated KO astrocyte co-cultures (Fig. 1g-i). Excitatory synapse formation (PSD-95/Bassoon colocalization) was also significantly restored in neurons exposed to peptide-treated KO astrocytes, reaching levels comparable to WT astrocyte co-culture conditions (55 ± 3.2% for WT-N + KO-A treated vs. untreated, 50.2 ± 4.1% for KO-N + KO-A treated vs. untreated) (Fig. 1j, k).Thus, peptide treatment of KO astrocytes is sufficient to restore their ability to support excitatory synaptogenesis and neuronal spine formation.

Consistent with the previously described lack of effect of KO-As on inhibitory synapse formation, peptide treatment of astrocytes had no effect on inhibitory synapses (SI Appendix, Fig. S1k, l). These data demonstrate that IGF1(1-3) peptide specifically restores excitatory synapse formation and neuronal spine formation by acting on KO astrocytes. To control for the possibility that IGF1 peptide in the media could diffuse from the insert membrane and act directly upon neurons, we also treated WT-N and KO-N with IGF1 peptide and found no changes in the number of excitatory or inhibitory synapses, indicating that the observed rescue requires astrocytes (Fig. 1j, k; SI Appendix, Fig. S1m). Thus, IGF1 peptide acts on astrocytes to restore their ability to support neuronal synaptogenesis.

These data demonstrate that peptide treatment of astrocytes alone, but not treatment of neurons, is sufficient to rescue excitatory synapse formation in neurons.

IGFBP2 is upregulated in KO astrocytes and their secretome

To identify secreted astrocytic factors responsible for reduced numbers of excitatory synapses, we performed quantitative proteomic profiling of both astrocyte-conditioned media (ACM) and whole-cell lysates from WT and KO astrocytes (WT-A and KO-A, Fig. 2a). This approach allowed us to examine both extracellular and intracellular alterations associated with MeCP2 loss.

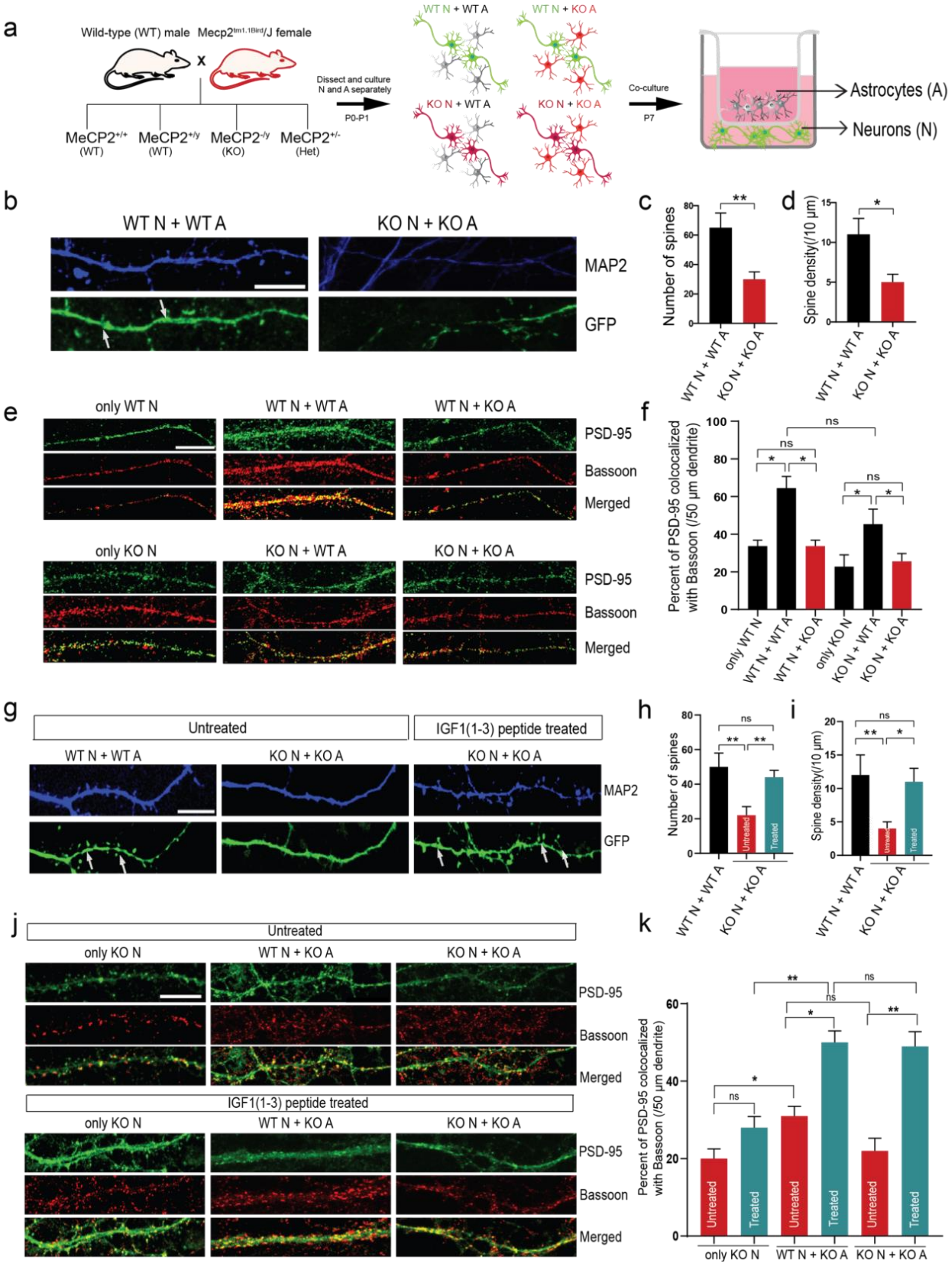

Fig. 1. MeCP2-deficient astrocytes impair excitatory synapse formation in neurons, which is rescued by IGF1(1-3) peptide treatment. (a) Schematic of the neuron-astrocyte co-culture system using wild-type (WT) or MeCP2 knockout (KO) neurons (N) and astrocytes (A), and experimental timeline. (b) Representative images of 50 µm segments of dendrites from WT N + WT A and KO N + KO A co-cultures stained for MAP2 (blue) and GFP (green) (scale bar = 10 µm). White arrows mark representative dendritic spines. (c–d) Quantification of total spine number (c) and spine density (spines/10 µm dendrite) (d). KO N + KO A co-cultures show reduced spine numbers and density compared to WT N + WT A ($**p < 0.01$, $*p < 0.05$; one-way ANOVA with Tukey's post hoc test; n = 4 cultures). (e) Representative images showing Bassoon (presynaptic marker, red), PSD-95 (postsynaptic marker, green), and merged channels in dendrites (scale bar = 10 µm). (f) Quantification of PSD-95/Bassoon colocalization (% per 50 µm dendrite; $*p < 0.05$; ns, non-significant; one-way ANOVA with Tukey's post hoc test; n = 6 cultures). (g) Representative images of MAP2 (blue) and GFP (green) in WT N + WT A and KO N + KO A, where KO A are untreated or treated with IGF1(1-3) peptide (100 ng/mL, 24 h). (h–i) Quantification showing that peptide treatment rescues spine number (h) and spine density (i) in KO N + KO A ($**p < 0.01$, $*p < 0.05$ vs. untreated KO; one-way ANOVA with Tukey's post hoc test). (j) Representative dendrite images from WT N + KO A and KO N + KO A co-cultures, untreated and peptide-treated (scale bar = 10 µm). (k) Quantification of excitatory synapse number in KO A co-cultures with or without peptide treatment ($*p < 0.05$, $**p < 0.01$ vs. untreated KO; one-way ANOVA with Tukey's post hoc test). All co-culture combinations were tested; representative conditions are shown for clarity.

Several insulin-like growth factor binding proteins (IGFBPs) were upregulated in both the media and cell lysates of KO-A. In ACM, IGFBP2 and IGFBP5 were among the most significantly increased proteins ($\log_2FC = 0.98$, adj. $p = 1.2 \times 10^{-3}$; $\log_2FC = 1.47$, adj. $p = 8.3 \times 10^{-3}$, respectively) (Fig. 2b, f and SI Appendix, Table S1). IGFBP2 was also elevated in whole-cell lysates ($\log_2FC = 0.74$, adj. $p = 7.8 \times 10^{-3}$). In addition, IGFBP4 was upregulated in KO astrocytes ($\log_2FC = 1.11$, adj. $p = 1.02 \times 10^{-5}$) (Fig. 2d, g and SI Appendix, Table S2). Together, these changes indicate a shared dysregulation of IGFBP levels and potentially of IGF1 signaling.

To determine the major pathways affected, we performed gene set enrichment analysis (GSEA) of ACM and astrocytic proteomes. GSEA revealed significant positive enrichment of an IGFBP-dependent pathway (Reactome) in ACM and a similar, though not statistically significant, enrichment in astrocytes (Fig. 2c, e and SI Appendix, Fig, S2a, b; Tables S3, S4).

Beyond IGF signaling, GSEA of KO ACM also showed activation of extracellular matrix (ECM)-related pathways (normalized enrichment score, NES = 1.51, FDR q = 0.002) and suppression of RNA metabolism (Reactome) (NES = -2.11, FDR q = 0.0009) (SI Appendix, Fig. S2a and Table S3). Likewise, GSEA of whole-cell astrocytic proteomes revealed dysregulation of metabolic processes, including mitochondrial matrix and cellular respiration, suggesting that MeCP2 deficiency also affects astrocyte metabolism (SI Appendix, Fig. S2b and Table S4). Notably, GSEA of secreted proteins also indicated suppression of nervous system development and Robo signaling pathways, which could impact neuronal synapse formation and maturation (SI Appendix, Fig. S2a).

To validate the proteomic results, we performed qPCR for multiple IGFBPs and synaptogenic genes. Igfbp1, Igfbp4, Igfbp5, Igfbp6, as well as EphA3 and Tnf, were significantly upregulated in KO astrocytes, whereas Igfbp2 mRNA was not elevated (SI Appendix, Fig. S2c). This discrepancy between mRNA and protein levels suggests that IGFBP2 is regulated post-translationally and that MeCP2 loss leads to an accumulation of the IGFBP2 protein. Collectively, these results identify IGFBP2 as a key protein upregulated in both ACM and astrocytes.

Peptide treatment reverses dysregulated proteins in MECP2-deficient astrocytes

To determine whether IGF1 peptide could reverse astrocytic proteome dysregulation, we performed differential proteomic analyses of KO astrocytes and ACM after 24 h of treatment with IGF1(1-3) peptide (100 ng/mL) (Fig. 3a). Comparison of protein fold changes between peptide-treated KO astrocytes and untreated KO vs. WT revealed that most significant proteomic alterations in KO astrocytes were at least partially reversed {75%, 2406/3216 significant differentially expressed proteins (DEPs) from KO vs. WT in the green quadrants}, with a strong negative correlation among all DEPs ($R = -0.57$, $p < 0.001$) (Fig. 3b). In contrast, ACM showed a smaller fraction of reversed proteins (52%, 359/691 total detected proteins in the green quadrants) and a weaker overall correlation ($R = -0.08$, $p < 0.01$) (Fig. 3c), indicating that the peptide primarily acts on intracellular rather than secreted protein networks (SI Appendix, Tables S1 and S2).

Because IGFBPs emerged as a shared class of upregulated proteins in both astrocytes and ACM, suggesting a coordinated alteration of IGF signaling, we next examined how IGF1(1-3) peptide treatment affects IGF pathway proteins. To visualize these changes, we extracted all detected IGF1 family members from the proteomic dataset and plotted their expression change profiles upon peptide treatment in astrocytes and ACM. In KO astrocytes, IGFBP2 and IGFBP4 were relatively downregulated after peptide treatment (Fig. 3b, d), whereas IGF protein levels in the ACM showed less prominent downregulation (Fig. 3c, e).

The impact of IGF1(1-3) peptide extended beyond individual IGFBPs. GSEA of treated vs. untreated ACM revealed partial restoration of several synaptic and IGF1 signaling pathways, although none reached statistical significance (SI Appendix, Table S5). In contrast, pathway reversal in KO astrocytes was more extensive and included several processes that did reach significance (SI Appendix, Table S6).

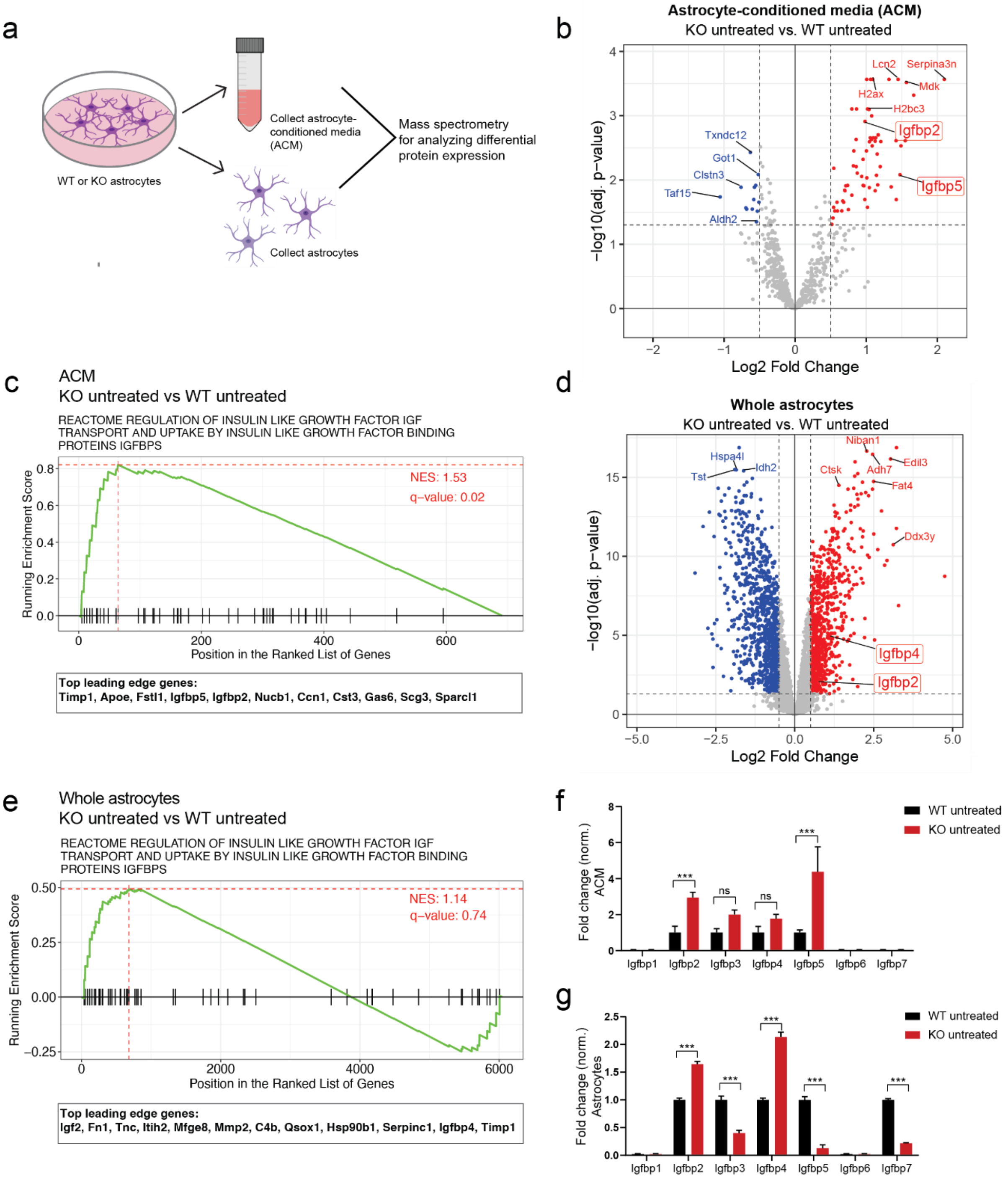

Fig. 2. IGFBPs are dysregulated in both MeCP2 KO astrocytes and astrocyte-conditioned media (ACM). (a) Workflow for mass spectrometry analysis of astrocyte-conditioned media (ACM) and cell lysates. (b) Volcano plot of differentially expressed proteins (DEPs) in ACM (KO vs. WT), highlighting upregulated proteins in red and downregulated proteins in blue. Note that Igfbp2 and Igfbp5 highlighted in the red box are upregulated ($\log_2 FC > 0.5$, adj. $p < 0.05$). (c) Gene set enrichment analysis shows significant positive enrichment of IGFBP-related pathway in KO ACM (NES = 1.53, q-val = 0.02). Leading edge genes driving this enrichment are indicated below. Dotted red lines indicate maximal magnitude enrichment score computed across proteins ranked by degree of differential expression in indicated comparison. Positive ES score indicates relative up-regulation of proteins in indicated pathway, corresponding to overrepresentation of pathway proteins (black ticks) at top of ranked protein list. (d) Volcano plot of DEPs in astrocytes (KO vs. WT), highlighting upregulated IGFBPs (red box; $\log_2 FC > 0.5$, adj. $p < 0.01$). (e) GSEA shows non-significant but still positive enrichment of IGFBP-related pathway in KO astrocytes (NES = 1.14, q-val = 0.74). Leading edge genes driving this enrichment are indicated below. (f, g) Fold change of IGFBPs in ACM (f) and astrocytes (g) (***, $p < 0.001$ vs. WT); ns, non-significant; two-tailed Student's t-test). NES = normalized enrichment score.

To summarize these trends, we selected our pathways of interest and plotted them side by side for each condition based on their absolute NES sum (SI Appendix, Fig. S3a-c and Table S5, S6). Consistent with the proteomic reversal plots, astrocytes displayed a broader restoration of neuron-synaptogenic and insulin/IGF-related pathways (SI Appendix, Fig. S3b, c), whereas ACM showed only limited recovery (SI Appendix, Fig. S3a). Note that in astrocytes, the IGFBP-related pathway that was earlier positively enriched was now reversed (SI Appendix, Fig. S3b).

Complementary western blot analyses reinforced these findings: IGFBP2 levels were significantly upregulated in KO-A and were strongly reduced following IGF1(1-3) peptide exposure, while other IGFBPs showed minimal changes (Fig. 3f, g). Importantly, IGFBP levels in KO-N remained unchanged before and after peptide exposure (SI Appendix, Fig. S3d, e), indicating that IGF1(1-3) peptide selectively targets astrocytic rather than neuronal IGFBP dysregulation in RTT.

Collectively, these results demonstrate that MeCP2-deficient astrocytes show aberrant upregulation of IGFBP2 in both intracellular and secreted compartments, and that IGF1(1-3) peptide treatment partially restores the astrocytic proteome by reversing IGFBP2 accumulation and rebalancing key IGF- and synapse-related pathways.

IGF1(1-3) peptide promotes proteasomal degradation of IGFBP2 and increases IGF1 bioavailability

IGFBP2 is known to bind IGF1 with high affinity, restricting its availability for receptor activation and thereby modulating downstream PI3K-Akt signaling (30-32). To investigate the mechanism underlying IGFBP2 regulation in RTT astrocytes, we tested whether IGF1(1-3) peptide affects the IGFBP2-IGF1 interaction. Co-immunoprecipitation (Co-IP) using FLAG-tagged full-length IGF1 (Fig. 4a) revealed that IGFBP2 binding to IGF1 was markedly elevated in KO astrocytes compared to WT (3.9 ± 0.5-fold over WT), and this binding was significantly reduced following peptide treatment (1.8 ± 0.7) (Fig. 4b, c). These findings indicate that IGF1(1-3) partially competes with IGFBP2 for IGF1 binding, thereby displacing the complex and potentially increasing IGF1 bioavailability for receptor engagement.

To identify additional protein complexes interacting with IGF1(1-3), we next performed a biotinylated IGF1(1-3) peptide pull-down followed by mass spectrometry (Fig. 4d). In WT astrocytes, peptide-associated complexes were most significantly enriched for mitochondrial proteins, whereas in KO astrocytes, proteasomal components were strongly enriched (Fig. 4e, f; SI Appendix, Table S7). These results suggested that the IGF1(1-3) peptide may promote proteasome-dependent turnover of IGFBP2.

Consistent with this hypothesis, we found that peptide treatment reduced IGFBP2 levels in KO astrocytes, and this reduction was blocked by the addition of proteasome inhibitor MG-132, confirming that IGFBP2 degradation requires proteasomal activity (Fig. 4g, h). Thus, IGF1(1-3) peptide likely acts through both mechanisms, displacing IGFBP2 from IGF1 to reduce sequestration and targeting IGFBP2 for proteasome-dependent degradation.

Finally, we tested the functional consequence of these mechanisms by measuring IGF1 levels in ACM by ELISA. KO ACM contained lesser IGF1 than WT (24.3 ± 1.7 vs. 52 ± 10.2 pg/mL). Importantly, peptide treatment significantly increased IGF1 levels in KO ACM (Fig. 4i). This demonstrates that IGF1(1-3) peptide not only reduces IGFBP2 abundance but also functionally rescues IGF1 bioavailability in the astrocytic environment, providing a direct link between IGFBP2 degradation and improved neuronal access to IGF1. Thus, IGF1(1-3) peptide regulates IGFBP2 through dual mechanisms: competitive displacement from IGF1 and proteasome-dependent degradation, thereby increasing IGF1 availability in astrocyte-conditioned medium.

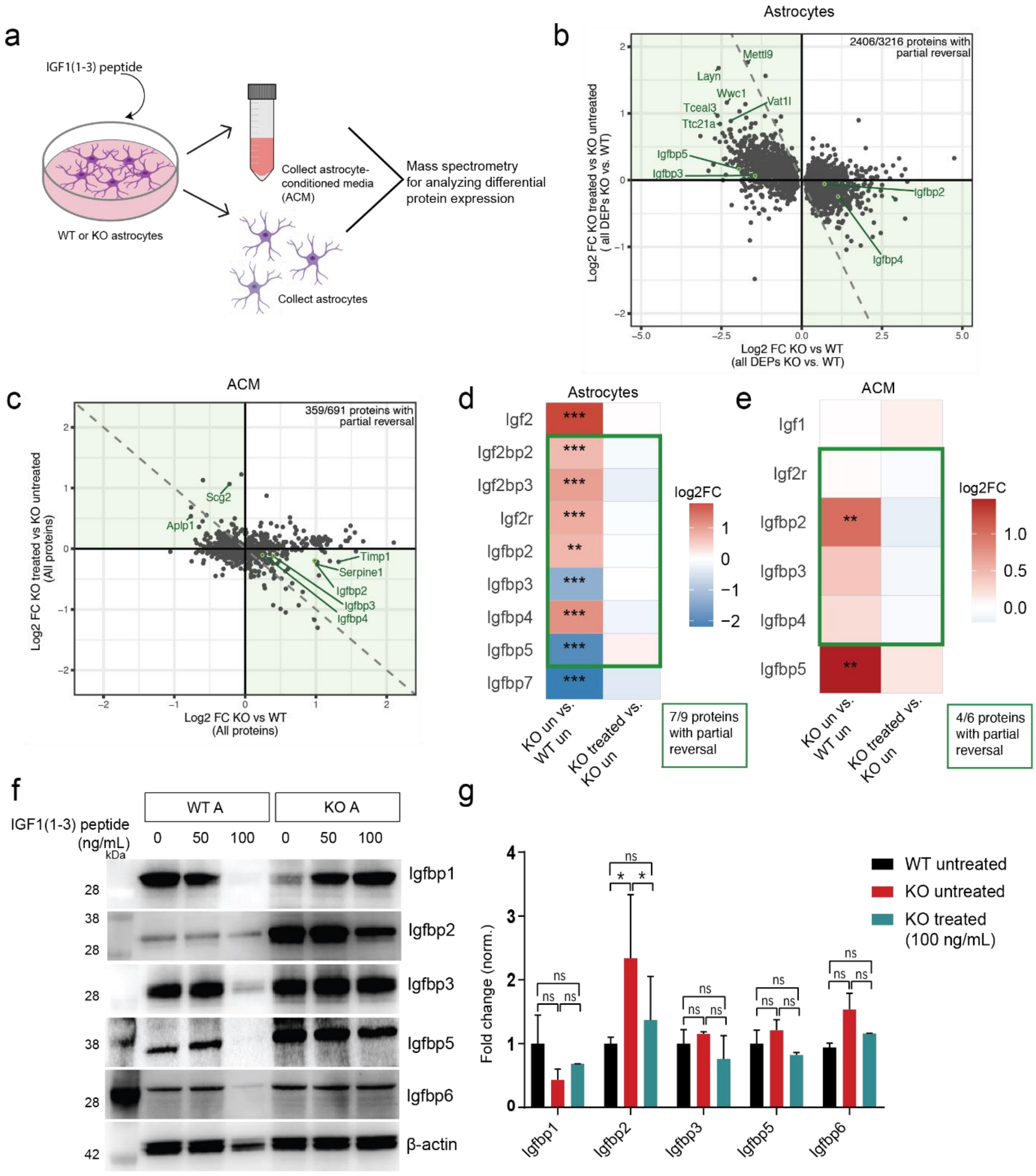

Fig. 3. IGF1(1-3) peptide treatment partially reverses dysregulated proteins in MeCP2-deficient astrocytes. (a) Experimental design for peptide treatment and proteomics. (b) Scatter plot of log$_2$FC (KO + peptide/KO) vs. log$_2$FC (KO/WT) in astrocytes for all DEPs in KO vs. WT (n = 3216), showing partial reversal for 2406/3216 proteins and strong anti-correlation (r = -0.57, $p < 0.001$). Reversed proteins fall in the green quadrants. Top left quadrant shows proteins that are decreased in KO untreated but increased in KO treated and the bottom right quadrant shows proteins that are increased in KO untreated but decreased in KO treated). (c) Scatter plot of log$_2$FC (KO + peptide/KO) vs. log$_2$FC (KO/WT) in ACM for all detected proteins (n = 691), showing partial reversal for 359/691 proteins (Pearson r = -0.08, $p < 0.01$). (d, e) Heatmaps of expression changes in IGF family proteins in astrocytes (e) and in ACM (f), proteins with statistically significant log$_2$FC values are indicated (log$_2$FC, KO vs. WT and KO+peptide vs. KO), * FDR < 0.05; ** FDR < 0.01; *** FDR < 0.001. (f) Western blot shows downregulation of upregulated IGFBP2 in treated vs. untreated KO astrocytes. (g) Quantification of Western blot (n = 3; *, $p < 0.05$). 100 ng/mL peptide was most effective. Only lane 1 or WT untreated was used as a control for all comparisons.

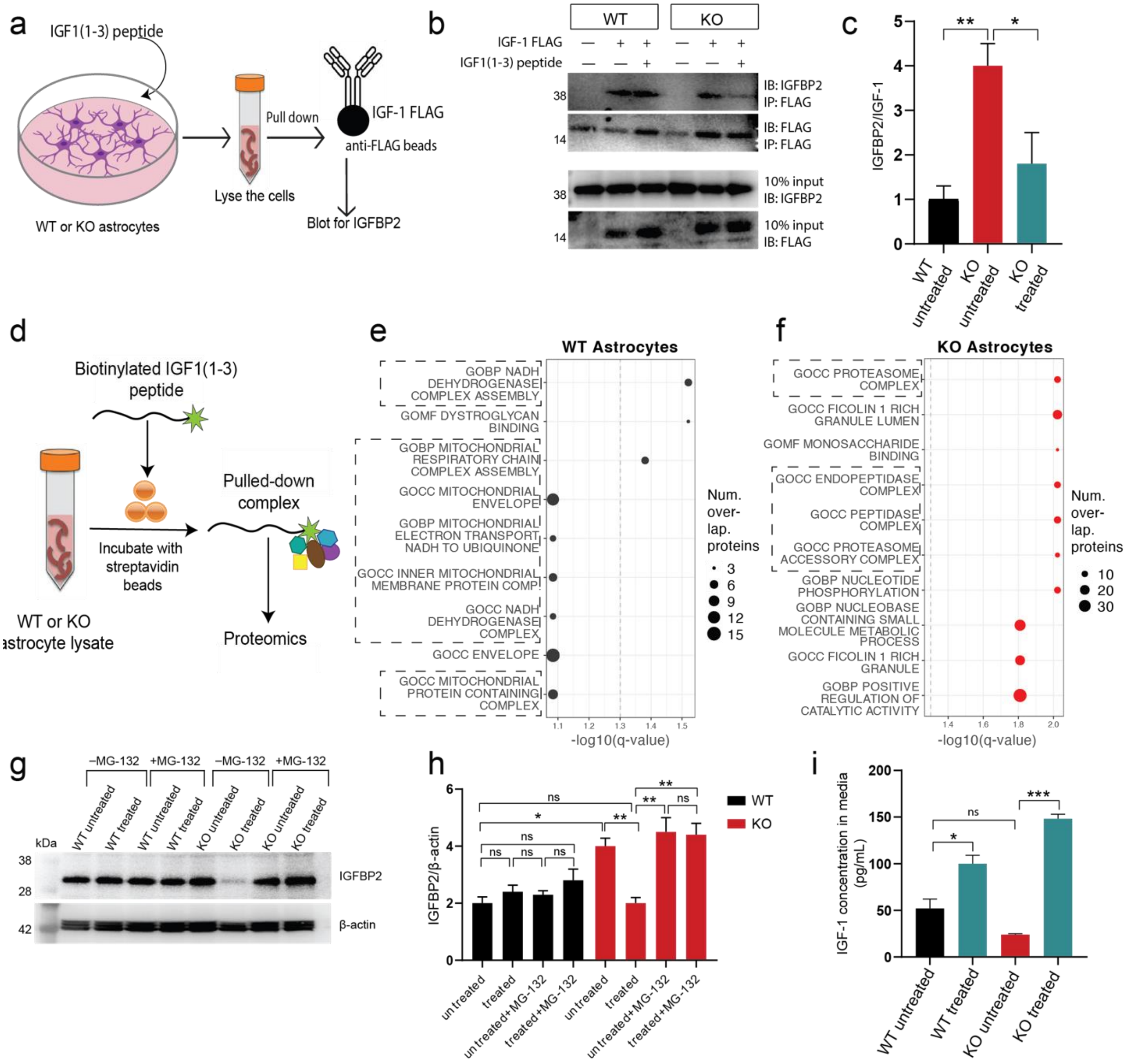

Fig. 4. Mechanism of IGF1 peptide action involves proteasomal degradation of IGFBP2, restoring free IGF1 bioavailability. (a) Co-immunoprecipitation experimental schematic using FLAG-tagged IGF1. (b) Representative Western blot of Co-IP samples probed for IGFBP2. (c) Quantification of IGFBP2 binding to IGF1 (n=3; **, $p < 0.01$; *, $p < 0.05$). (d) Workflow for biotinylated IGF1(1-3) peptide pull-down and mass spectrometry. (e, f) Gene Ontology (GO) term analysis of proteins enriched in biotinylated IGF1(1-3) pull-downs from WT astrocytes (mitochondrial, respiration terms indicated) (e) and KO astrocytes (proteasome, peptidase terms indicated) (f). (g) Western blot of IGFBP2 levels in KO astrocytes treated with IGF1(1-3) peptide in the presence or absence of proteasome inhibitor MG-132. (h) Quantification of IGFBP2 levels from (g) (n=3; *, $p < 0.05$; **, $p < 0.01$; ns, not significant). (i) Free IGF1 levels measured by ELISA in astrocyte-conditioned media (ACM) from WT, KO, and KO + peptide conditions (n=4; ***, $p < 0.001$).

IGF1(1-3) peptide reverses IGFBP2-linked mitochondrial dysfunction in MeCP2 KO astrocytes

While biotinylated IGF1(1-3) peptide pull-down proteomics revealed that KO-A were enriched in proteasomal components, WT-A were enriched in mitochondrial proteins (Fig. 4e). To investigate how IGFBP2 dysregulation affects mitochondrial pathways, we evaluated the KO-A proteome before and after IGF1(1-3) peptide treatment (Fig. 5a). GSEA revealed that KO-A vs. WT-A proteomic changes show a significant negative enrichment score for several metabolic pathways, including cellular respiration and oxidative phosphorylation pathways (Fig. 5a). Peptide treatment was able to reverse the enrichment scores for most of these pathways and 46/50 leading edge proteins contributing to the negative enrichment of oxidative phosphorylation showed partial reversal upon peptide treatment (Fig. 5a, b; SI Appendix, Tables S2, S6).

Since IGFBP2 and other IGFBPs are known to affect mitochondrial structure and function, we curated several IGF1-mitochondria composite gene sets to specifically examine mitochondrial proteins that are regulated by IGF1 and IGFBP2 based on published literature (33-35). We evaluated known pathway proteins including: (i) IGFBP2-integrin/FAK-Akt signaling, (ii) PTEN-autophagy/mitophagy components, and (iii) IGF1-dependent mitochondrial protective pathways (NRF2-BNIP3, PGC-1α-NRF1/TFAM modules). Most of these pathways were systematically dysregulated in KO astrocytes and partially restored by peptide treatment, although we note that enrichment scores for these pathways did not reach statistical significance (Fig. 5c).

In particular, leading edge analysis of the oxidative phosphorylation compact gene set revealed that 12/12 proteins were partially reversed by IGF1(1-3) treatment (Fig. 5d). These included proteins such as Ndufa9, Atp5f1a, and Atp5f1b. Because several of these are direct Akt or AMPK targets, IGFBP2-integrin/FAK-Akt signaling is mechanistically linked (36).

To directly relate these proteomic shifts to mitochondrial physiology, we examined functional and morphological changes in mitochondria. MitoTracker imaging revealed reduced mitochondrial number and size, as well as mean MitoTracker intensity in KO astrocytes (Fig. 5e-h). All of these deficits were rescued in astrocytes treated with IGF1(1-3) peptide (Fig. 5e-h). Furthermore, seahorse extracellular flux analysis showed significantly decreased basal and maximal oxygen consumption rates (OCR) and extracellular acidification rate (ECAR) in KO astrocytes compared to WT. Again, peptide treatment of astrocytes restored ECAR and OCR rates to near WT levels (Fig. 5i, j). Finally, ATP bioluminescent assay showed that peptide treatment of KO-A increased extracellular ATP two-fold, rescuing ATP release to WT levels after treatment (Fig. 5k).

Taken together, these findings suggest that elevated IGFBP2 in MeCP2-deficient astrocytes disrupts IGF1-linked mitochondrial signaling pathways, resulting in the suppression of mitochondrial OXPHOS proteins, impaired mitochondrial morphology, reduced respiration, and reduced ATP release. Treatment of astrocytes with IGF1(1-3) peptide promotes proteasome-dependent degradation of IGFBP2, restores IGF1 availability, rescues mitochondrial proteomic networks, and normalizes mitochondrial physiology in astrocytes.

IGF1(1-3) peptide treatment targeted to astrocytes rescues neuronal growth and synaptogenesis by normalizing IGF1 signaling and synaptic protein expression in neurons

To determine the molecular consequences of astrocyte-targeted IGF1(1-3) peptide treatment on neurons, we performed quantitative proteomic analysis of neurons co-cultured with either untreated or peptide-treated KO astrocytes (KO-A) (Fig. 6a). Several proteins were differentially expressed in KO neurons co-cultured with untreated KO-A compared to WT co-cultures, including P2rx7 (ATP receptor), while treatment of KO-A with IGF1(1-3) reversed changes in proteins such as Homer3 (postsynaptic protein) (SI Appendix, Fig. S4a, b; Table S8). Notably, IGF1(1-3) had no significant effect on the proteome of KO neurons cultured in isolation, confirming that the rescue is mediated importantly via astrocytes (SI Appendix, Fig. S4c).

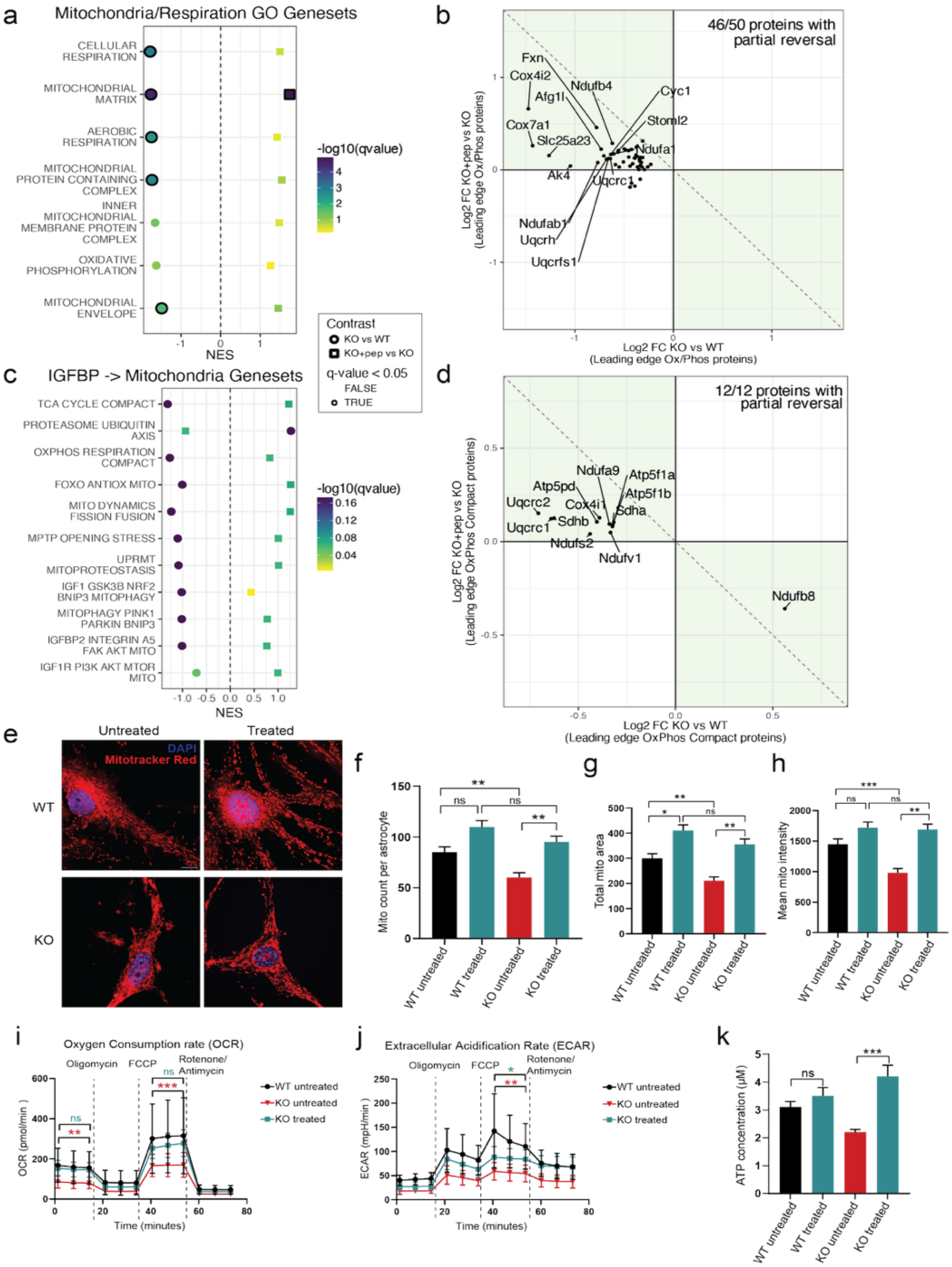

Fig. 5. IGF1(1-3) peptide rescues mitochondrial dysfunction in MeCP2 KO astrocytes. (a) GSEA normalized enrichment score plot showing top mitochondrial-related pathways suppressed in KO vs. WT astrocytes (left) and their positive enrichment in KO astrocytes treated with peptide vs. untreated (right). Pathways include cellular respiration, mitochondrial inner membrane, mitochondrial protein-containing complex, and oxidative phosphorylation. Different shapes denote the two conditions and color indicates the q-value; x-axis represents normalized enrichment score (NES). Significant pathway enrichments are indicated with black borders. (b) Scatter plot of leading-edge oxidative phosphorylation proteins showing reversal in protein expression changes upon peptide treatment of KO-A. (c) GSEA normalized enrichment score plot for IGF1 and IGFBP regulated mitochondrial pathways. Several pathways show nominal reversal of NES in KO + peptide vs. KO. (d) Leading edge analysis identifying 12/12 "oxphos compact" proteins reversed by peptide treatment. (e) Representative images of WT and KO astrocytes, untreated or peptide-treated, stained with Mitotracker Red CMXRos (mitochondria, red) and DAPI (nuclei, blue) Scale bar = 10 µm. (f-h) Quantification of mitochondrial number per cell (f), total mitochondrial area per cell (g), and mean mitochondrial fluorescence intensity (h) from Mitotracker images (n = 5 independent cultures; *, $p < 0.05$; **, $p < 0.01$; ***, $p < 0.001$; one-way ANOVA with Tukey's post hoc test). (i, j) Seahorse extracellular flux analysis of oxygen consumption rate (OCR; pmol/min) (i) and extracellular acidification rate (ECAR; mpH/min) (j) in WT and KO astrocytes with or without peptide. OCR and ECAR are significantly reduced in KO astrocytes and are restored toward WT levels after treatment (*, $p < 0.05$; **, $p < 0.01$; ***, $p < 0.001$; ns, non-significant). (k) ATP concentration in astrocyte-conditioned media (µM), showing decreased release from KO astrocytes and significant rescue upon peptide treatment (***, $p < 0.001$; one-way ANOVA with Tukey's post hoc test).

GSEA analysis comparing neurons co-cultured with peptide-treated versus untreated KO-A revealed top pathways showing significant reversal based on their absolute NES scores (SI Appendix, Table S9). We focused on pathways associated with synapse assembly, dendritic spine formation, and IGF1-dependent signaling. While several pathways did not reach statistical significance, they still exhibited opposite enrichment trends (Fig. 6b, d). Neurons co-cultured with untreated KO-A displayed suppression of pathways essential for excitatory synapse assembly, dendritic spine morphogenesis, and synaptic plasticity (Fig. 6b). Treatment with IGF1(1-3) showed activation of these pathways, with key reversed leading-edge proteins including DLG4 (PSD-95) and GRIA1 (AMPA receptor subunit) (Fig. 6c).

Further, GSEA of these expression changes also demonstrated reversal in enrichment scores in pathways related to IGF1/IGF1R signaling, with leading-edge proteins such as AKT1, MAPK3, and MAPK1 (ERK1/2) normalized following peptide treatment (Fig. 6d, e). These changes are particularly relevant, as Akt and ERK1/2 are critical downstream effectors of the IGF1/insulin pathway. Additional proteins showing reversed fold changes included IGF1R (IGF1 receptor), AKT2, NTRK2 (BDNF receptor), and DLGAP1 (postsynaptic density protein) (SI Appendix, Fig. S4d). Western blot validation confirmed increased PSD-95 and phosphorylated Akt (p-Akt) levels in neurons co-cultured with treated KO-A, consistent with restoration of postsynaptic integrity and downstream IGF1 pathway activation (Fig. 6f-i).

These data demonstrate that IGF1(1-3) peptide treatment, by targeting MeCP2-deficient astrocytes, broadly and at least partially normalizes the neuronal proteome, restoring fundamental developmental programs, rebalancing key signaling pathways such as PTEN/PI3K/Akt, and rescuing synaptic and mitochondrial protein networks.

Finally, to test the therapeutic relevance of these findings *in vivo*, we administered IGF1(1-3) peptide daily (0.02 mg/g, i.p.) from postnatal day 18-28 in WT, global MeCP2-null (MeCP2$^{-/y}$), and astrocyte-specific conditional KO mice (Aldh1l1-Cre; MeCP2$^{-/y}$) (SI Appendix, Fig. S5a). Open field tests showed that locomotor activity deficits in both models were significantly improved with peptide treatment (SI Appendix, Fig. S5b, c). In rotarod assays, motor learning deficits were partially rescued in astrocyte-specific KO mice but remained impaired in global nulls (SI Appendix, Fig. S5d), suggesting that some motor deficits can be ameliorated by IGF1(1-3) peptide potentially targeting astrocytic MeCP2, whereas others may be refractory to such treatment.

Taken together, our findings support a model in which MeCP2-deficient astrocytes upregulate IGFBP2, which sequesters IGF1 and limits neuronal PI3K-Akt signaling, PSD95 expression, and excitatory synaptogenesis. Treatment with the IGF1(1-3) peptide hampers IGFBP2 interaction with full-length IGF1 and promotes its proteasomal degradation, thereby restoring IGF1 bioavailability to neurons. Importantly, our proteomics and Western analyses indicate that this dual mechanism restores both neuronal signaling (PI3K/Akt/mTOR, PSD95 levels) and astrocytic metabolic support (mitochondrial structure, OXPHOS proteins, ATP release) (Fig. 7).

Discussion

Rett syndrome (RTT) is a devastating neurodevelopmental disorder caused by loss-of-function mutations in *MECP2* (37-40). While traditionally considered a neuron-centric disorder, growing evidence highlights astrocytes as critical non-cell-autonomous regulators of RTT pathology (24, 25, 29, 41). Here, we identify astrocyte-secreted IGFBP2 as a molecular brake on synaptogenesis regulated by MeCP2-deficient astrocytes and show that treatment with IGF1(1-3) peptide degrades IGFBP2, restores IGF1 availability, rescues mitochondrial and metabolic support, and normalizes neuronal PI3K-Akt-PSD95 signaling. These findings provide a mechanistic explanation for the efficacy of IGF1(1-3) and potentially for its mimetic Trofinetide, the first FDA-approved drug for RTT (20).

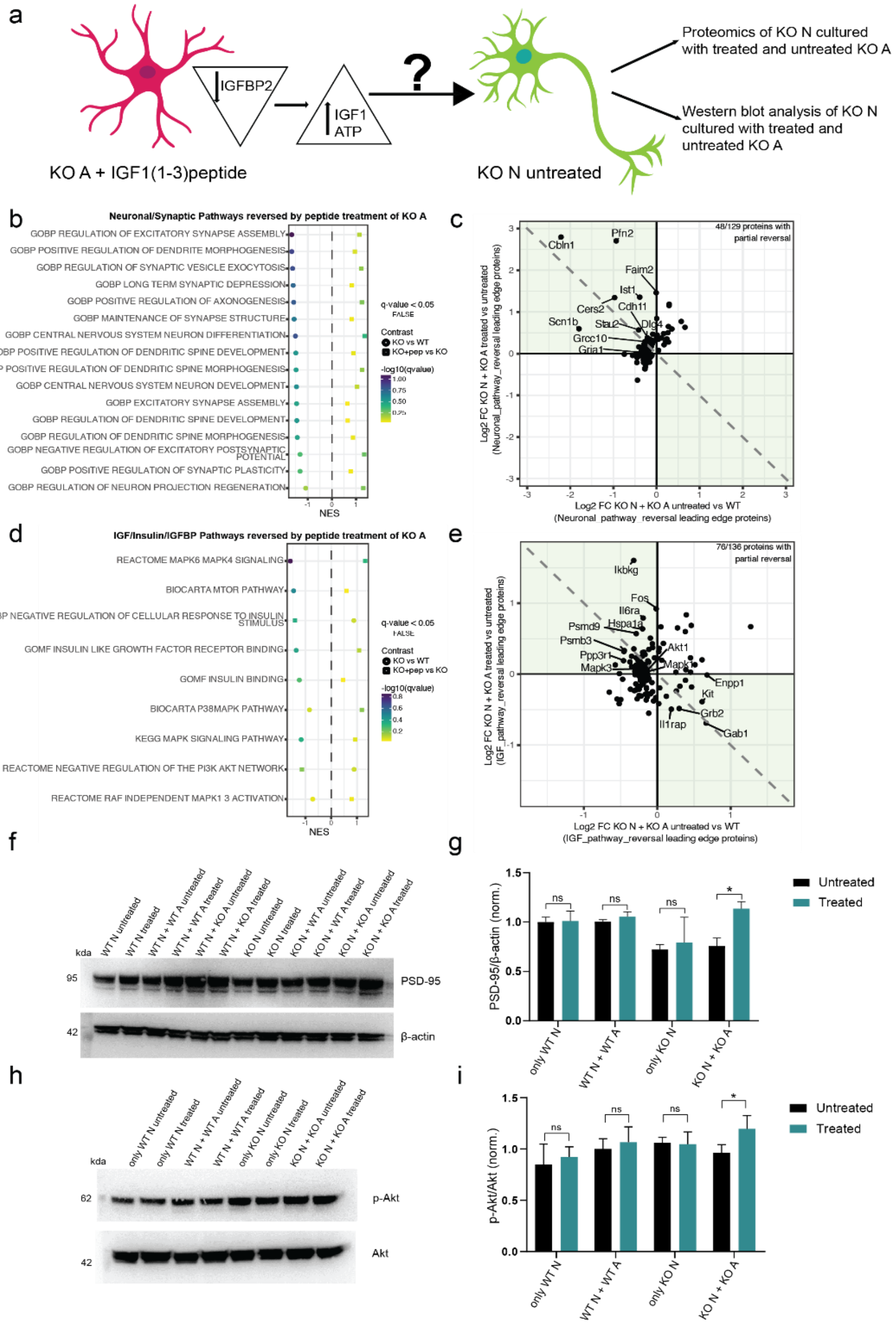

Fig. 6. IGF1 peptide treatment of astrocytes restores synaptic protein levels and IGF1 downstream signaling pathways in neurons. (a) Schematic illustrating experimental design and logic. IGF1(1-3) treatment of KO-A leads to downregulation of IGFBP2 and increase in IGF1 and ATP levels in the media. To answer how these changes affect KO-N, they were co-cultured with treated or untreated WT- or KO-A and neuronal proteomes were analyzed to assess astrocyte-mediated effects. (b) GSEA normalized enrichment score plot of neuronal/synaptic pathways nominally reversed by peptide treatment of KO-A in co-culture, highlighting partial restoration of dendritic spine development, excitatory synapse assembly, and synaptic plasticity. (c) Scatter plot of leading-edge proteins from neuronal/synaptic pathways that exhibit partial or complete reversal following peptide treatment (48/129 proteins show partial reversal; green-shaded region). (d) GSEA normalized enrichment score plot of IGF/insulin/IGFBP-related pathways nominally reversed in neurons co-cultured with peptide-treated KO-A. (e) Scatter plot of leading-edge proteins from IGF/insulin/IGFBP-related pathways with reversal following peptide treatment (76/136 proteins show partial reversal; green-shaded region). (f-i) Western blot validation and quantification of selected neuronal proteins. (f, g) PSD-95 and β-actin levels showing restoration of postsynaptic density protein expression in KO-N co-cultured with treated KO-A. (g, h) Phospho-Akt and total Akt levels confirming reactivation of downstream IGF1 signaling in neurons following IGF1(1-3) peptide exposure. Data represent mean ± SEM (n = 3 independent cultures; * $p < 0.05$, ** $p < 0.01$; one-way ANOVA with Tukey's post-hoc test).

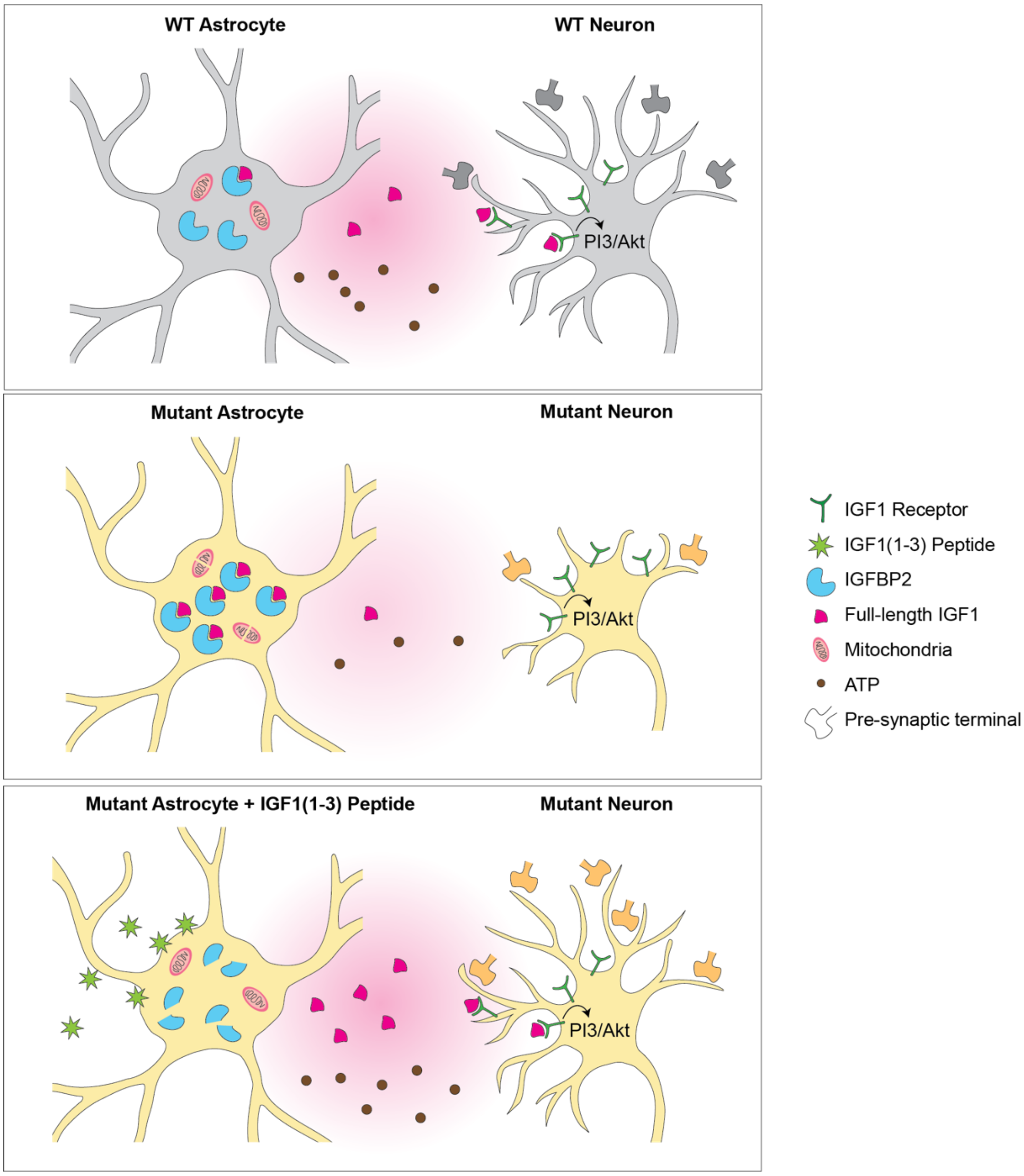

Fig. 7. Proposed model of astrocyte-mediated synaptic and mitochondrial dysfunction in MeCP2 deficiency and rescue by IGF1(1-3) peptide. WT astrocytes secrete IGF1 and ATP that supports neurite outgrowth and synaptogenesis in WT neurons. KO astrocytes overexpress IGFBP2, that sequesters IGF1 and breaks down mitochondria, thus impairing neuronal PI3K-Akt signaling and synaptogenesis. Loss of mitochondrial integrity and function in KO astrocytes is accompanied with decreased ATP production. IGF1(1-3) peptide treatment of KO astrocytes degrades IGFBP2 and restores mitochondrial integrity and function, thus rescuing ATP release and IGF1 bioavailability, which in turn rescues neuronal PI3/Akt signaling and restores synapse formation.

The bidirectional regulation of IGFBP2 and IGF1 signaling illustrates the dual roles of MeCP2 as transcriptional repressor and activator (5-7, 9). In astrocytes, MeCP2 mutations cause increased expression of IGFBP2 (29; this study), consistent with the role of MeCP2 as transcriptional repressor. At the same time, IGF1 signaling and its downstream pathway in neurons is downregulated, as is BDNF signaling (13, 42-44), consistent with the role of MeCP2 as transcriptional activator. The reduction of IGF1 signaling is at least partially due to increased IGFBP2, which binds IGF1 and reduces its availability, and supplying exogenous IGF1 can partially rescue symptoms and IGF1 signaling in neurons of Rett model mice (14, 30). While the application of IGF1 peptide also partially rescues symptoms and IGF1 signaling (13), an open question has been why IGF1(1-3) peptide mimics the effects of IGF1 despite evidence that it does not engage the IGF1 receptor (IGF1R) with the same affinity or in the same manner as full-length

IGF1 (45, 46). Our study provides a plausible explanation: rather than acting directly on neurons, IGF1(1-3) promotes proteasomal degradation of IGFBP2 in astrocytes. By removing this inhibitory binding protein, IGF1 is made available to engage neuronal receptors and trigger canonical PI3K-Akt-S6 and PSD95/GluA1 signaling cascades. This mechanism clarifies how IGF1(1-3) converges functionally with IGF1 on synaptic outcomes, despite differences in receptor interactions.

Our study also contributes to a growing body of work exploring the mechanisms by which astrocytes regulate neuronal development. Consistent with previous studies showing that astrocytes secrete synaptogenic molecules such as thrombospondins, hevin, and glypicans (47, 48), we find that MeCP2-deficient astrocytes also secrete synapse-suppressive cues, including IGFBP2 and other ECM regulators. It is reasonable to propose that IGFBP2 upregulation sequesters IGF1, disrupts PI3K-Akt signaling, and leads to a loss of PSD-95 and other synaptic proteins in neurons. We show that IGF1 peptide treatment rescues PSD-95 levels, Homer3 expression, and Akt signaling, suggesting that the peptide restores not only synaptic structure but also functional IGF1 signaling cascades. These findings align with *in vivo* observations that IGF1 analogs improve synaptic function, plasticity and behavioral outcomes in RTT mouse models (13, 14) and provide direct mechanistic evidence of how astrocyte-mediated IGF1 signaling modulates neuronal circuit assembly.

Interestingly, our study did not find significant changes in inhibitory synapse formation as shown by gephyrin/Bassoon colocalization across genotypes or treatment conditions (SI Appendix, Fig. S1e, f; Fig. S1l, m). Similar effect was seen previously upon IGF1(1-3) treatment of neurons (49). This suggests that astrocytic MeCP2 loss preferentially affects excitatory synapse development, possibly due to selective regulation of excitatory synaptogenic proteins. These results support the excitation-inhibition imbalance seen in RTT (50, 51). Alternatively, inhibitory circuits may be less sensitive to IGFBP2-mediated IGF1 sequestration, or the time frame of treatment (24 h) may not be sufficient to induce observable changes. These observations warrant deeper investigation into the circuit- and cell-type-specific responses to astrocyte-mediated IGF1 signaling.

Our data also highlight a second dimension of astrocytic dysfunction, viz. impaired mitochondrial support. MeCP2-deficient astrocytes displayed fragmented mitochondria, reduced oxygen consumption, and diminished ATP release. These physiological deficits map directly onto suppressed expression of mitochondrial oxidative phosphorylation (OXPHOS) proteins and mitochondrial regulators (e.g., Ndufs6, Atp5a1, Cox6b1, Mfn2, Mdh1, Idh1), which were consistently downregulated in KO astrocytes and restored by peptide treatment. Many of these proteins are direct Akt or AMPK targets, positioning IGFBP2-integrin/FAK-Akt signaling as a mechanistic link between IGFBP2 dysregulation and mitochondrial health (30, 33, 36, 52). While our functional assays focused on OCR and ATP release, the concordant reversal of OXPHOS proteins by IGF1(1-3) provides molecular evidence that mitochondrial function is directly tied to IGFBP2 regulation. This integrated path from proteomics to physiology strengthens the case that astrocytic metabolism is an essential contributor to RTT pathology.

Interestingly, mitochondrial proteins were among the top interactors of IGF1(1-3) in WT astrocytes but were replaced by proteasomal proteins in MeCP2 KOs (Fig. 4e, f), suggesting a shift in cellular priorities from energy production to proteostasis. Previous studies have implicated mitochondrial dysfunction in RTT pathology (27, 53, 54), and our work expands this view by positioning astrocytes, and specifically IGFBP2 dysregulation, as a contributing factor. Notably, neutralizing IGFBP2 in RTT ACM has been shown to rescue dendritic outgrowth in neurons (29), supporting our conclusion that astrocyte-secreted IGFBP2 is a core molecular brake on neuronal maturation. Protein accumulation is a hallmark of several neurodevelopmental and neurodegenerative disorders, and our study suggests that Trofinetide may also recruit the proteasomal machinery and restore protein balance.

Notably, the astrocyte-specific conditional knockout experiments support the concept of astrocytes as therapeutic targets for neurodevelopmental and other disorders. IGF1(1-3) peptide treatment improved locomotion and partially rescued motor learning in these mice, whereas global MeCP2-null mice showed only partial behavioral rescue. Indeed, IGF1(1-3) treatment has been shown previously to improve a range of phenotypes including breathing variability, heart rate, locomotion and life span in MeCP2-null mice (13). Prior work showed that genetic restoration of MeCP2 in astrocytes improved locomotion and breathing patterns in MeCP2-null mice (26). Thus, several key phenotypes can be ameliorated through astrocytic rescue, though different brain regions that mediate specific functions may be differentially amenable to such rescue.

Our study has several limitations. First, although our proteomics and functional assays established a strong link between IGFBP2 and mitochondrial support, more detailed biochemical validation (e.g., Western blots or immunostaining for individual OXPHOS proteins) would strengthen the pathway-level claims. Second, we did not directly quantify astrocyte- versus neuron-specific IGFBP2 levels *in vivo* before and after peptide treatment. Third, while our *in vivo* experiments provide proof-of-concept behavioral rescue, they were limited in scope; future work should expand to systemic and behavioral endpoints which are clinically relevant in RTT.

Together, these findings identify astrocytic IGFBP2 as a central mediator of non-cell-autonomous dysfunction in Rett syndrome and provide a mechanistic explanation for the efficacy of IGF1(1-3) peptide in treating RTT. By promoting proteasomal degradation of IGFBP2, the peptide enhances IGF1 signaling to neurons and normalizes astrocytic mitochondrial support, thereby rescuing both synaptic and metabolic deficits. This dual action highlights astrocytes not simply as passive contributors but as active gatekeepers of neuronal circuit maturation. From a translational perspective, IGFBP2 is potentially both a therapeutic target and a biomarker of treatment response. More broadly, our work emphasizes that targeting astrocytic dysfunction is sufficient to restore neuronal signaling and behavior, supporting the paradigm of cell-type-specific interventions for neurodevelopmental disorders. Future studies aimed at astrocyte-selective delivery of IGF1 mimetics, or direct modulation of IGFBP2 and its downstream signaling pathways, may thus open new avenues for durable, mechanism-based therapies in Rett syndrome and related conditions.

Materials and Methods

Animals

All animal experiments were approved by the Institutional Animal Care and Use Committee (CAC) at the Massachusetts Institute of Technology and conducted in accordance with the National Institutes of Health guidelines. Wild-type (WT) and Mecp2-null mice (B6.129P2(C)-Mecp2$^{tm1.1Bird/J}$, Stock #: 003890) were obtained from The Jackson Laboratory. Astrocyte-specific conditional knockout (cKO) mice were generated by crossing floxed Mecp2 mice with Aldh1l1-Cre mice (The Jackson Laboratory, Stock #: 023748). Both male and female pups were used for *in vitro* experiments; only male animals were used for *in vivo* behavioral studies.

Primary Cell Culture

Astrocyte Cultures. Cortical astrocytes were isolated from postnatal day 1-3 (P1-P3) WT or Mecp2-null mice. Cortices were dissected, meninges removed, and tissue dissociated in 0.05% trypsin-EDTA (Thermo Fisher). Cells were plated in Astrocyte media (ScienCell Technologies) with 10% fetal bovine serum (FBS) and 1% penicillin-streptomycin and maintained for 10-14 days. Confluent monolayers were shaken at 130-150 rpm in an orbital shaker to remove microglia and oligodendrocyte precursor cells, then replated for downstream assays. Pups were genotyped by PCR prior to tissue collection.

Neuron-Astrocyte Co-culture System. Cortical neurons were isolated from P0 mice and seeded on poly-D-lysine-coated coverslips at a density of 125,000 cells per well in 24-well plates. After 3 d *in vitro* (DIV3), fluorodeoxyuridine (FuDr) (Sigma) was added to inhibit glial proliferation. For indirect co-culture, astrocytes were plated on transwell inserts in Neurobasal medium (Thermo Fisher) and suspended above neuronal monolayers. Co-culture was maintained for 7-10 d in Neurobasal medium supplemented with B27, GlutaMAX, and antibiotic-antimycotic. For all experiments, four conditions were used: WT neurons (WT-

N) + WT astrocytes (WT-A), WT-N + KO-A, KO-N + WT-A, and KO-N + KO-A (Fig. 1a). All the combinations were analyzed, representative conditions are shown for clarity and to avoid overcrowding of the figure. IGF1(1-3) peptide treatment was performed at DIV7 for 24 h prior to setting up the co-cultures.

Peptide Treatment

A synthetic IGF1(1-3) peptide (Gly-Pro-Glu; GPE) was obtained from Bachem and reconstituted in sterile water. Astrocytes or neurons were treated with 100 ng/mL peptide for 24 h unless otherwise specified. Co-cultures were established 24 h after peptide treatment. To control for potential effects of IGF1(1-3) peptide diffusion across the transwell membrane, only WT- or KO-treated astrocyte or neuron (A or N) conditions were used. Dose-response experiments (50-200 ng/mL; SI Appendix, Fig. S1i, j) confirmed that 100 ng/mL was appropriate for all functional assays. For proteasome inhibition, cells were co-treated with MG-132 (10 µM; Sigma-Aldrich) for 4 h.

Immunocytochemistry and Spine Analysis

Cells were fixed with 4% (vol/vol) paraformaldehyde (PFA), permeabilized with 0.1% Triton X-100, and blocked with 5% (vol/vol) normal goat serum. Primary antibodies included rabbit anti-MAP2 (1:500; Abcam), mouse anti-GFAP (1:500; Millipore), rabbit anti-PSD-95 (1:500; Sigma), guinea pig anti-Bassoon (1:500; Synaptic Systems), mouse anti-Gephyrin (1:500; Synaptic Systems), and rabbit anti-GFP (1:500; Abcam). Species-specific secondary antibodies conjugated to Alexa Fluor dyes (Thermo Fisher) were used. Images were acquired on a Leica SP8 confocal microscope and analyzed in FIJI/ImageJ. Spine number and density were quantified along secondary dendrites over 50-µm segments from 10-15 neurons per condition (Fig. 1c, d).

Western Blotting

Cells or tissues were lysed in RIPA buffer containing protease and phosphatase inhibitors. Protein concentration was determined by BCA assay. Equal protein amounts were separated by SDS/PAGE, transferred to PVDF membranes, and probed with antibodies against MeCP2 (1:1000; Cell Signaling Technology), PSD-95 (1:1000; Cell Signaling Technology), IGFBP2 and other IGFBPs (1:1,000; R&D Systems), Phospho-p44/42 MAPK (Erk 1/2) (1:1000; Cell Signaling Technology), FLAG (1:200; Sigma), p44/42 MAPK (Erk 1/2) (1:1000; Cell Signaling Technology), Phospho-Akt (Ser473) (1:1000; Cell Signaling Technology), Akt (1:1000; Cell Signaling Technology), and β-actin (1:2000; Sigma). Blots were visualized by ECL (Millipore) on a ChemiDoc (Bio-Rad) and quantified by densitometry in ImageJ.

Coimmunoprecipitation (Co-IP)

pLV CMV IGF1-FLAG was a gift from Larry Gerace (Addgene plasmid # 175170). WT and KO astrocytes were transfected with the full-length FLAG-tagged IGF1 expression plasmid using Lipofectamine 3000 (Thermo Fisher). After 24 h of treatment with 100 ng/mL IGF1(1-3) peptide, cells were lysed, and Co-IP was performed using anti-FLAG M2 agarose beads (Sigma). Precipitates were washed, eluted, and probed for IGFBP2 by Western blot.

Proteomics

Sample Preparation. Conditioned media (ACM) and astrocyte lysates were collected after 24 h of serum-free incubation (with or without peptide treatment). Samples were concentrated and protein was digested using trypsin. Peptides were desalted using C18 spin columns and submitted for DIA or TMT analysis.

Data-Independent Acquisition (DIA) Mass Spectrometry. Cell supernatants and cell pellets were lysed in SDC lysis buffer (1% (w/v) SDC, 100mM TEAB pH 8.5, 40mM CAA, 10mM TCEP) and heated at 70 °C for 15 min in Low Protein Binding Microcentrifuge Tubes (Thermo Fisher Scientific, Waltham, MA, USA). Samples were centrifuged at 16,000 x g for 10 min and resulting supernatants were transferred to fresh low-bind tubes. Proteins were proteolytically digested overnight in a shaking incubator at 37 °C at 115 RPM with trypsin/LysC mix (1:100) in 100mM TEAB. The following day, an additional dose of trypsin/LysC mix was added (1:100) in 100mM TEAB and the digestion proceeded for 4 hours at 37 °C. Peptide digests were purified using SDB-RPS Stage Tips (55). The peptides were then dried using a Speed-Vac concentrator and reconstituted in 12 µL 0.2 % (v/v) formic acid in MS-grade water for LC-MS analysis.

Mass spectrometry was performed using an Orbitrap Eclipse mass spectrometer equipped with a FAIMS Pro interface connected to a Vanquish Neo chromatography system, all from Thermo Fisher Scientific (Waltham, MA, USA). Chromatographic separation utilized an EasySpray ES902 column (75 µm x 25 cm, 100 Å) from Thermo Fisher Scientific. Peptide extracts were injected with a volume of 2 µL. Peptide separation was conducted with a mobile phase consisting of 0.1% (v/v) formic acid in water (solution A) and 0.1% (v/v) formic acid in 80% (v/v) acetonitrile (solution B), flowing at 300 nL/min, while the column temperature was held constant at 30 °C. Peptides were separated on a gradient of 3-25% B for 45 min, 25-40% B for 15 min, 40-95% B for 5 min, 95% B over 6 min.

Using the MS in positive mode, the ion source temperature was set to 305 °C, and ionized peptides passed through the FAIMS Pro unit at -50 V. Mass spectra were collected in MS1 mode with a resolution of 120,000 with a scan range of 350-2000 m/z. Standard automatic gain control and automatic injection time setting were used. For MS2 data collection, the mass spectrometer was operated in DIA mode with a resolution of 30,000. MS2 spectra were gathered across a precursor mass range of m/z 375-1200, utilizing isolation windows of m/z 25, with 0.5 m/z overlaps, a custom AGC target (AGC = 1000%), and 30% CID collision energy.

Proteomic analysis was conducted using DIA-NN version 1.8 (56). Raw LC-MS data files were processed in library-free mode, utilizing an in silico-digested Mus musculus FASTA database (UniProt Taxon ID: UP000000589). The search was configured for Trypsin/P cleavage specificity, allowing a maximum of one missed cleavage and enabling removal of N-terminal methionine. Carbamidomethylation of cysteine residues was specified as a fixed modification. Peptide lengths were limited to between 7 and 30 amino acids, with precursor ion charge states restricted to +2 through +4. The precursor ion mass-to-charge (m/z) range was set to 300-1800 and that one of fragment ions was set from 200 to 1800. A precursor-level false discovery rate (FDR) of 1.0% was applied. DIA-NN was executed with isotopologue detection enabled, gene-level protein inference, and settings for heuristic protein interference handling and exclusion of shared spectra. The built-in neural network classifier was operated in single-pass mode. Data normalization was turned on, and spectral library generation was performed using the smart profiling feature. The analysis was configured to optimize computational efficiency with respect to processing speed and memory usage. Protein spreadsheets were exported as .csv files and processed for downstream analysis (57).

Tandem Mass Tag (TMT) Mass Spectrometry. Supernatants and cell pellets were lysed in SDC lysis buffer (1% (w/v) SDC, 100mM TEAB pH 8.5, 40mM CAA, 10mM TCEP) and heated at 70 °C for 15 min in Low Protein Binding Microcentrifuge Tubes (Thermo Fisher Scientific, Waltham, MA, USA). Proteins were extracted via the SP3 method (58). Briefly, proteins were bound to SP3 beads by adding a 4X volume of 100% (v/v) ethanol followed by three washing steps with 80% (v/v) ethanol in LC-MS grade water. Proteins were proteolytically digested overnight in a shaking incubator at 37 °C at 115 RPM with trypsin/LysC mix (1:100) in 100mM TEAB. The following day, an additional dose of trypsin/LysC mix was added (1:100) in 100mM TEAB and the digestion proceeded for 4 hours at 37 °C.

Peptides were dried in a speed-vac concentrator and reconstituted in 200 mM TEAB. Peptides were labeled with TMTpro reconstituted in anhydrous acetonitrile by adding the label in 100 µg increments, incubating for 1 hour at RT after addition of each dose. TMTpro-labeled samples were quenched for 30 min at RT with 5% hydroxylamine in 100mM TEAB. Samples were pooled and dried in a speed-vac concentrator. The pooled sample was fractionated using a Strong Anion Exchange column (Thermo Scientific, Waltham, MA, USA). Increasing concentrations of ammonium acetate (0, 20, 50, 100, 200, 500 mM) were used for elution. Low salt fractions (0, 20, 50 mM ammonium acetate) and high salt fractions (100, 200, 500 mM ammonium acetate) were pooled respectively and lyophilized. The pooled high-salt and low-salt fractions were each then fractionated further with the High pH Reversed-Phase Peptide

Fractionation Kit (Thermo Scientific, Waltham, MA, USA) using the following 12-step gradient of increasing acetonitrile concentrations: 5, 7.5, 10, 12.5, 15, 17.5, 20, 22.5, 25, 27.5, 30, 60%. The following fractions were then pooled together and lyophilized: 1+7, 2+8, 3+9, 4+10, 5+11, 6+12. Lyophilized fractions were resuspended in 12 µL 0.2% formic acid in MS-grade water for LC-MS analysis.

Mass spectrometry was performed using an Orbitrap Eclipse mass spectrometer equipped with a FAIMS Pro source connected to an Vanquish Neo nLC chromatography system, all from Thermo Fisher Scientific (Waltham, MA, USA). Chromatographic separation utilized an EasySpray ES902 column (75 µm x 25 cm, 100 Å) from Thermo Fisher Scientific at 300 nl/min on a gradient of 3-25% B over 90 min, 25-40% B over 30 min, 40-95% B over 10 min, with a column wash at 95% B for 6 min, using 0.1% FA in water for A and 0.1% FA in 80% acetonitrile for B. The Orbitrap and FAIMSpro were operated in positive ion mode with a positive ion voltage of 2100 V, an ion transfer tube temperature of 305°C, and a 4.2 L/min carrier gas flow, using standard FAIMS resolution and compensation voltages of -45, -55, and -65 V. Full scan spectra were acquired at a resolution of 120,000 (MS1) and 50,000 (MS2), with a scan range of 400-1400 m/z, automatic maximum fill time, custom AGC target (300% MS1, 250% MS2), isolation windows of m/z 0.7, intensity threshold of 2.0e4, 2-6 charge state, dynamic exclusion of 60 seconds, and 38% HCD collision energy.

Mass spectrometry data were analyzed using PEAKS Studio version 10.6. Raw data files underwent scan merging with a 10 ppm retention time tolerance and a 10 ppm precursor mass window, focusing on precursor charge states ranging from +2 to +8. Initial data preprocessing included scan merging, automatic centroiding, deisotoping, and deconvolution of MS spectra. Protein identification was carried out using the UniProt reference proteome for Mus musculus (UP000000589). Search parameters were set with a parent ion mass tolerance of 15 ppm and a fragment ion mass tolerance of 0.05 Da. Trypsin was specified as the protease with semi-specific cleavage (D/P) allowed, accommodating up to three missed cleavage sites. Variable modifications included carbamidomethylation of cysteines and oxidation of methionine residues, with a maximum of three variable modifications permitted per peptide. A decoy-fusion approach was used to estimate and control the false discovery rate (FDR), with peptide and protein identifications filtered to achieve an FDR of ≤1%, and a significance threshold set at -10lgP ≥ 20. Quantitative protein values were determined by averaging the intensities of at least two of the most abundant peptides identified per protein for each TMTpro channel using the Peaks Q Module. Quantified results were exported as .csv files and processed for downstream analysis following the methodology described earlier.

Statistical analysis and preprocessing

Normalization and filtering of protein intensity measurements for all experiments was performed using a standard pipeline as implemented in DEP (59). Samples with an outlying number of missing values (>1.5 interquartile ranges from first or third quartiles) were removed. Proteins with missing values in both WT and KO samples were filtered out, except for in neuron/astrocyte coculture experiments, where a maximum threshold of 5 missing values across WT and KO samples was set. Protein intensity values were log2-transformed and normalized through variance stabilizing transformation as implemented in DEP.

Differential Analysis

Differential analysis was performed using R/Bioconductor software package, limma, and resulting p-values were Benjamini-Hochberg corrected. Visualizations (volcano plots) were generated with ggplot2, and differentially expressed proteins (DEPs) were filtered by log2 fold change > 0.5 and adjusted p < 0.05 for visualization.

Gene set enrichment analyses (GSEA)

Gene set enrichment analysis (60, 61) was performed to determine relative enrichment of pathway associated proteins among all proteins in differential analysis results. Briefly, for each differential contrast tested, proteins were ranked by their signed p-value, defined as $\log_2FC$ * -log10(p-value). A running enrichment score (ES) for each pathway set was computed by iterating through this ranked list and increasing the score when a protein from the set was encountered. The maximal recorded ES (by magnitude) indicates the degree to which each protein set is overrepresented at either extreme of the differential analysis. Permutation tests are used to generate an empirical null ES distribution and assign p-values. Raw ES values were then normalized to account for gene set size.

Gene set enrichment analysis (GSEA) overrepresentation analyses were performed using clusterProfiler (v.4.8.2) with pathway sets from Gene Ontology (GO), Kyoto Encyclopedia of Genes and Genomes (KEGG), and Reactome, downloaded through msigdbr (v.7.5.1). Tested gene sets include pathway sets from Gene Ontology (GO), KEGG, and Reactome, downloaded through the msigdbr (v.7.5.1) package, along with literature-curated gene sets as defined in earlier sections. GSEA was performed using the clusterProfiler package (v.4.8.2). Visualizations were generated with ggplot2 (v.3.5.1).

Biotinylated Peptide Pull-Down and Mass Spectrometry

Biotinylated IGF1(1-3) peptide (biotin at N-terminus) was synthesized through Genscript. It was incubated with Dynabeads streptavidin beads (ThermoFisher) for 24 hr. Cells were lysed and peptide-protein complexes were isolated using streptavidin-coated magnetic beads. Protein-bound magnetic beads were resuspended in 100µL 100mM TEAB with 40mM CAA and 10mM TCEP in MS-grade water and reduced and alkylated at 70 °C for 15 min in Low Protein Binding Microcentrifuge Tubes (Thermo Fisher Scientific, Waltham, MA, USA). 1 µg trypsin/Lys-C mix was added in 1 µL 100mM TEAB and bead suspensions were digested overnight in a shaking incubator at 37 °C at 115 RPM. The following day, 1 µg trypsin/LysC mix was added in 1 µL 100mM TEAB and the digestion continued at 37 °C for 4 hours.

Peptides were dried in a speed-vac concentrator and reconstituted in 200 mM TEAB. Peptides were labeled with TMTpro resuspended in anhydrous acetonitrile by adding the label in 100 µg increments, incubating for 1 hour at RT after addition of each dose. TMTpro-labeled samples were quenched for 30 min at RT with 5% hydroxylamine in 100mM TEAB. Samples were pooled and dried in a speed-vac concentrator. The pooled sample was then fractionated using the High pH Reversed-Phase Peptide Fractionation Kit (Thermo Scientific, Waltham, MA, USA) following the 8-step elution gradient for TMT-labeled peptides. The resulting fractions were lyophilized and resuspended in 12 µL 0.2% formic acid in MS-grade water for LC-MS analysis.

Mass spectrometry was performed using an Orbitrap Eclipse mass spectrometer equipped with a FAIMS Pro source connected to an Vanquish Neo nLC chromatography system, all from Thermo Fisher Scientific (Waltham, MA, USA). Chromatographic separation utilized an Aurora Ultimate TS25 column (75 µm x 25 cm, 120 Å) from IonOpticks (Fitzroy, VIC, AUS) at 300 nl/min on a gradient of 3-25% B over 90 min, 25-40% B over 30 min, 40-95% B over 10 min, with a column wash at 95% B for 6 min, using 0.1% FA in water for A and 0.1% FA in 80% acetonitrile for B. The Orbitrap and FAIMSpro were operated in positive ion mode with a positive ion voltage of 2100 V, an ion transfer tube temperature of 305°C, and a 4.2 L/min carrier gas flow, using standard FAIMS resolution and compensation voltages of -45 and -60 V. Full scan spectra were acquired at a resolution of 120,000 (MS1) and 50,000 (MS2), with a scan range of 400-1400 m/z, automatic maximum fill time, custom AGC target (300% MS1, 250% MS2), isolation windows of m/z 0.7, intensity threshold of 2.0e4, 2-6 charge state, dynamic exclusion of 60 seconds, and 38% HCD collision energy.

Mass spectrometry data were analyzed using PEAKS Studio version 10.6. Raw data files underwent scan merging with a 10 ppm retention time tolerance and a 10 ppm precursor mass window, focusing on precursor charge states ranging from +2 to +8. Initial data preprocessing included scan merging, automatic centroiding, deisotoping, and deconvolution of MS spectra. Protein identification was carried out using the UniProt reference proteome for Mus musculus (UP000000589). Search parameters were set with a parent ion mass tolerance of 15 ppm and a fragment ion mass tolerance of 0.05 Da. Trypsin was specified as the protease with semi-specific cleavage (D/P) allowed, accommodating up to three missed cleavage sites. Variable modifications included carbamidomethylation of cysteines and oxidation of methionine residues, with a maximum of three variable modifications permitted per peptide. A decoy-fusion approach was used to estimate and control the false discovery rate (FDR), with peptide and protein identifications filtered to achieve an FDR of ≤1%, and a significance threshold set at -10lgP ≥ 20. Quantitative protein values were determined by averaging the intensities of at least two of the most abundant peptides identified per protein for each TMTpro channel using the Peaks Q Module. Quantified results were exported as .csv files and processed for downstream analysis following the methodology described earlier.

Statistical analysis

Normalization and filtering of protein intensity measurements for pulldown analysis was performed with DEP as described earlier (Proteomics Preprocessing). Significant protein interactors in both WT and KO astrocytes were determined using limma (biotinylated vs. control, $\log_2 FC > 0$, adj. $p\text{-value} < 0.05$). GO term overrepresentation analysis was performed using clusterProfiler and msigdbr packages.

Mitochondrial Imaging and Functional Assays

Mitotracker Staining

Cells were stained with MitoTracker Red CMXRos (100 nM, Thermo Fisher) and DAPI (1 μg/mL) for 30 min at 37°C. Images were acquired by confocal microscopy. Mitochondrial area, intensity, and count were quantified using custom ImageJ macros.

Seahorse Metabolic Assay

Oxygen consumption rate (OCR) and extracellular acidification rate (ECAR) were measured using a Seahorse XF Analyzer (Agilent) following the Mito Stress Test protocol. Parameters included basal respiration, ATP production, and spare respiratory capacity.

ATP Quantification

Extracellular ATP levels were measured using a luciferase-based assay (ATP Bioluminescence Kit, Abcam) and normalized to cell number.

ELISA

IGF1 levels in ACM were measured using a mouse IGF1 ELISA kit (Thermo Fisher) according to the manufacturer's instructions. Samples were run in technical duplicates and analyzed on a plate reader at 450 nm.

RNA Isolation and qPCR

RNA was extracted (RNeasy kit; Qiagen), and cDNA was synthesized (Takara). qPCR was performed using SYBR Green Master Mix on a QuantStudio system. Gene expression was normalized to *Gapdh* (ΔΔCt method).

Behavioral Studies

Male Mecp2-null and Aldh1l1-Cre;Mecp2$^{flox/y}$ mice received daily i.p. injections of IGF1(1-3) peptide (0.02 mg/g) or vehicle from P18 to P28. Behavioral tests were conducted at P29-30.

Open Field Test. Locomotor activity was tracked for 15 min using Bonsai software.

Rotarod. Mice were tested on an accelerating rotarod (4-40 rpm over 5 min) over 3 days; latency to fall was recorded.

Statistical Analysis

Data are presented as mean ± SEM. Group comparisons were made using unpaired two-tailed Student's t-tests or one-way ANOVA followed by Tukey's post hoc test. $p < 0.05$ was considered statistically significant. Statistical analyses were performed using GraphPad Prism.

Acknowledgements

We thank Taylor Johns for technical and administrative support. We thank Jiho Park for assistance in preparing Fig. 7. We thank Brooke Linnehan from the Whitehead proteomics core for her assistance with the proteomics experiments. This research was supported by NIH training grant T32MH112510 (R.M.L.), International Rett Syndrome Foundation (D.L.T), NIH grant RF1AG075901 (E.F.), NIH grant 5R01MH104610 (R.J.), NIH grant R01MH085802 and the Simons Foundation Autism Research Initiative (SFARI) (M.S.).

Author Contributions

Conceptualization: P.O., M.S.; Methodology: P.O., V.K., F.S.; Investigation: P.O., A.B., F.S., R.M.L.; Formal analysis: P.O., V.K., F.S.; Visualization: P.O., V.K.; Resources: V.K., D.L.T., M.S.; Funding acquisition: M.S.; Supervision: E.F., R.J., M.S.; Writing-original draft: P.O., V.K.; Writing-review & editing: P.O., V.K., R.M.L., M.S.

References

1. R. E. Amir, *et al.*, Rett syndrome is caused by mutations in X-linked MECP2, encoding methyl-CpG-binding protein 2. *Nat Genet* **23**, 185-188 (1999).
2. M. Chahrour, H. Y. Zoghbi, The Story of Rett Syndrome: From Clinic to Neurobiology. *Neuron* **56**, 422-437 (2007).
3. M. J. Lyst, *et al.*, Rett syndrome mutations abolish the interaction of MeCP2 with the NCoR/SMRT co-repressor. *Nature Neuroscience* **16**, 898-902 (2013).
4. M. J. Lyst, A. Bird, Rett syndrome: A complex disorder with simple roots. *Nat Rev Genet* **16**, 261-275 (2015).
5. J. P. K. Ip, N. Mellios, M. Sur, Rett syndrome: insights into genetic, molecular and circuit mechanisms. *Nature Reviews Neuroscience* **19**, 368-382 (2018).
6. Y. Liu, *et al.*, Exploring the complexity of MECP2 function in Rett syndrome. *Nature Reviews Neuroscience* **26**, 379-398 (2025).
7. M. Chahrour, *et al.*, MeCP2, a Key Contributor to Neurological Disease, Activates and Represses Transcription. *Science* **320**, 1224-1229 (2008).
8. L. Chen, *et al.*, MeCP2 binds to non-CG methylated DNA as neurons mature, influencing transcription and the timing of onset for Rett syndrome. *Proc Natl Acad Sci U S A* **112**, 5509-5514 (2015).
9. Y. Liu, *et al.*, MECP2 directly interacts with RNA polymerase II to modulate transcription in human neurons. *Neuron* **112**, 1943-1958 (2024).
10. J. Guy, J. Gan, J. Selfridge, S. Cobb, A. Bird, Reversal of Neurological Defects in a Mouse Model of Rett Syndrome. *Science* **315**, 1143-1147 (2007).
11. E. Giacometti, S. Luikenhuis, C. Beard, R. Jaenisch, Partial rescue of MeCP2 deficiency by postnatal activation of MeCP2. *Proc Natl Acad Sci U S A* **104**, 1931-1936 (2007).

12. D. Tropea, *et al.*, Gene expression changes and molecular pathways mediating activity-dependent plasticity in visual cortex. *Nature Neuroscience* **9**, 660-668 (2006).

13. D. Tropea, *et al.*, Partial reversal of Rett Syndrome-like symptoms in MeCP2 mutant mice. *Proc Natl Acad Sci U S A* **106**, 2029-2034 (2009).

14. J. Castro, *et al.*, Functional recovery with recombinant human IGF1 treatment in a mouse model of Rett Syndrome. *Proc Natl Acad Sci U S A* **111**, 9941-9946 (2014).

15. J. Castro, N. Mellios, M. Sur, Mechanisms and therapeutic challenges in autism spectrum disorders: insights from Rett syndrome. *Curr Opin Neurol* **26**, 154-159 (2013).

16. A. Banerjee, J. Castro, M. Sur, A. E. West, O. Khwaja, Rett syndrome: genes, synapses, circuits, and therapeutics. *Front Psychiatry* **3**, 34 (2012).

17. A. Banerjee, M. T. Miller, K. Li, M. Sur, W. E. Kaufmann, Towards a better diagnosis and treatment of Rett syndrome: a model synaptic disorder. *Brain* **142**, 239-248 (2019).

18. J. L. Neul, *et al.*, Trofinetide for the treatment of Rett syndrome: a randomized phase 3 study. *Nature Medicine* **29**, 1468-1475 (2023).

19. A. K. Percy, *et al.*, Trofinetide for the treatment of Rett syndrome: Results from the open-label extension LILAC study. *Med* **5**, 1178-1189 (2024).

20. Z. U. N. Mughal, *et al.*, Trofinetide receives FDA approval as first drug for Rett syndrome. *Annals of Medicine and Surgery* **86**, 2382-2385 (2024).

21. E. C. Williams, *et al.*, Mutant astrocytes differentiated from Rett syndrome patients-specific iPSCs have adverse effects on wild-type neurons. *Hum Mol Genet* **23**, 2968-2980 (2014).

22. E. Albizzati, *et al.*, Mecp2 knock-out astrocytes affect synaptogenesis by interleukin 6 dependent mechanisms. *iScience* **27** (2024).

23. F. M. Postogna, O. M. Roggero, F. Biella, A. Frasca, Interpreting the rich dialogue between astrocytes and neurons: An overview in Rett syndrome. *Brain Res Bull* **227**, 111386 (2025).

24. N. Ballas, D. T. Lioy, C. Grunseich, G. Mandel, Non-cell autonomous influence of MeCP2-deficient glia on neuronal dendritic morphology. *Nature Neuroscience* **12**, 311-317 (2009).

25. I. Maezawa, S. Swanberg, D. Harvey, J. M. LaSalle, L. W. Jin, Rett Syndrome Astrocytes Are Abnormal and Spread MeCP2 Deficiency through Gap Junctions. *Journal of Neuroscience* **29,** 5051-5061 (2009).

26. D. T. Lioy, *et al.*, A role for glia in the progression of Rett's syndrome. *Nature* **475**, 497-500 (2011).

27. D. L. Tomasello, *et al.*, Mitochondrial dysfunction and increased reactive oxygen species production in MECP2 mutant astrocytes and their impact on neurons. *Scientific Reports* **14**, 20565 (2024).

28. J. Sun, *et al.*, Mutations in the transcriptional regulator MeCP2 severely impact key cellular and molecular signatures of human astrocytes during maturation. *Cell Rep* **42**, 111942 (2023).

29. A. L. M. Caldwell, *et al.*, Aberrant astrocyte protein secretion contributes to altered neuronal development in multiple models of neurodevelopmental disorders. *Nat Neurosci* **25**, 1163-1178 (2022).

30. R. C. Baxter, Signaling Pathways of the Insulin-like Growth Factor Binding Proteins. *Endocr Rev* **44**, 753-778 (2023).

31. S. M. Firth, R. C. Baxter, Cellular actions of the insulin-like growth factor binding proteins. *Endocr Rev* **23**, 824-854 (2002).

32. T. Sitar, G. M. Popowicz, I. Siwanowicz, R. Huber, T. A. Holak, Structural basis for the inhibition of insulin-like growth factors by insulin-like growth factor-binding proteins. *Proc Natl Acad Sci U S A* **103**, 13028-13033 (2006).

33. C. C. Feng, *et al.*, Hypoxia suppresses myocardial survival pathway through HIF-1α-IGFBP-3-dependent signaling and enhances cardiomyocyte autophagic and apoptotic effects mainly via FoxO3a-induced BNIP3 expression. *Growth Factors* **34**, 73-86 (2016).

34. V. C. Russo, W. J. Azar, S. W. Yau, M. A. Sabin, G. A. Werther, IGFBP-2: The dark horse in metabolism and cancer. *Cytokine Growth Factor Rev* **26**, 329-346 (2015).

35. S. Riis, J. B. Murray, R. O'Connor, IGF-1 Signalling Regulates Mitochondria Dynamics and Turnover through a Conserved GSK-3β-Nrf2-BNIP3 Pathway. *Cells* **9**, 147 (2020).

36. X. Wang, *et al.*, IGFBP2 induces podocyte apoptosis promoted by mitochondrial damage via integrin α5/FAK in diabetic kidney disease. *Apoptosis* **29**, 1109-1125 (2024).

37. H. Y. Zoghbi, Rett syndrome: what do we know for sure? *Nat Neurosci* **12**, 239-240 (2009).

38. V. R. B. Liyanage, M. Rastegar, Rett syndrome and MeCP2. *Neuromolecular Med* **16**, 231-264 (2014).

39. D. Feldman, A. Banerjee, M. Sur, Developmental Dynamics of Rett Syndrome. *Neural Plast* **2016**, 6154080 (2016).

40. K. V. Good, J. B. Vincent, J. Ausió, MeCP2: The Genetic Driver of Rett Syndrome Epigenetics. *Front Genet* **12**, 620859 (2021).

41. U. Kahanovitch, K. C. Patterson, R. Hernandez, M. L. Olsen, Glial Dysfunction in MeCP2 Deficiency Models: Implications for Rett Syndrome. *Int J Mol Sci* **20**, 3813 (2019).

42. Z. Zhou, *et al.*, Brain-Specific Phosphorylation of MeCP2 Regulates Activity-Dependent Bdnf Transcription, Dendritic Growth, and Spine Maturation. *Neuron* **52**, 255-269 (2006).

43. Q. Chang, G. Khare, V. Dani, S. Nelson, R. Jaenisch, The disease progression of Mecp2 mutant mice is affected by the level of BDNF expression. *Neuron* **49**, 341-348 (2006).

44. W. G. Chen, *et al.*, Derepression of BDNF Transcription Involves Calcium-Dependent Phosphorylation of MeCP2. *Science* **302**, 885-889 (2003).

45. J. Saura, *et al.*, Neuroprotective effects of Gly-Pro-Glu, the N-terminal tripeptide of IGF-1, in the hippocampus in vitro. *Neuroreport* **10**, 161-164 (1999).

46. J. Guan, H. J. Waldvogel, R. L. M. Faull, P. D. Gluckman, C. E. Williams, The effects of the N-terminal tripeptide of insulin-like growth factor-1, glycine-proline-glutamate in different regions following hypoxic-ischemic brain injury in adult rats. *Neuroscience* **89**, 649-659 (1999).

47. K. S. Christopherson, *et al.*, Thrombospondins are astrocyte-secreted proteins that promote CNS synaptogenesis. *Cell* **120**, 421-433 (2005).

48. H. Kucukdereli, *et al.*, Control of excitatory CNS synaptogenesis by astrocyte-secreted proteins Hevin and SPARC. *Proceedings of the National Academy of Sciences* **108**, E440-E449 (2011).

49. A. P. Corvin, *et al.*, Insulin-like growth factor 1 (IGF1) and its active peptide (1-3)IGF1 enhance the expression of synaptic markers in neuronal circuits through different cellular mechanisms. *Neurosci Lett* **520**, 51-56 (2012).

50. W. Li, Excitation and Inhibition Imbalance in Rett Syndrome. *Front Neurosci* **16**, 825063 (2022).

51. A. Banerjee, *et al.*, Jointly reduced inhibition and excitation underlies circuit-wide changes in cortical processing in Rett syndrome. *Proc Natl Acad Sci U S A* **113**, E7287-E7296 (2016).

52. Y. Jia, *et al.*, Interaction of insulin-like growth factor-binding protein-3 and BAX in mitochondria promotes male germ cell apoptosis. *Journal of Biological Chemistry* **285**, 1726-1732 (2010).

53. M. T. Dotti, *et al.*, Mitochondrial dysfunction in Rett syndrome. *Brain Dev* **15**, 103-106 (1993).

54. N. Shulyakova, A. C. Andreazza, L. R. Mills, J. H. Eubanks, Mitochondrial Dysfunction in the Pathogenesis of Rett Syndrome: Implications for Mitochondria-Targeted Therapies. *Front Cell Neurosci* **11**, 58 (2017).

55. J. Rappsilber, M. Mann, Y. Ishihama, Protocol for micro-purification, enrichment, pre-fractionation and storage of peptides for proteomics using StageTips. *Nature Protocols* **2**, 1896-1906 (2007).

56. V. Demichev, C. B. Messner, S. I. Vernardis, K. S. Lilley, M. Ralser, DIA-NN: neural networks and interference correction enable deep proteome coverage in high throughput. *Nature Methods* **17**, 41-44 (2019).

57. F. Schulte, H. Hasturk, M. Hardt, Mapping Relative Differences in Human Salivary Gland Secretions by Dried Saliva Spot Sampling and nanoLC-MS/MS. *Proteomics* **19**, 1900023 (2019).

58. C. S. Hughes, *et al.*, Single-pot, solid-phase-enhanced sample preparation for proteomics experiments. *Nature Protocols* **14**, 68-85 (2019).

59. X. Zhang, *et al.*, Proteome-wide identification of ubiquitin interactions using UbIA-MS. *Nature Protocols* **13**, 530-550 (2018).

60. A. Subramanian, *et al.*, Gene set enrichment analysis: A knowledge-based approach for interpreting genome-wide expression profiles. *Proc Natl Acad Sci U S A* **102**, 15545-15550 (2005).

61. G. Korotkevich, *et al.*, Fast gene set enrichment analysis. *bioRxiv* 060012 [Preprint] (2016). https://www.biorxiv.org/content/10.1101/060012v3

Supplementary Figures

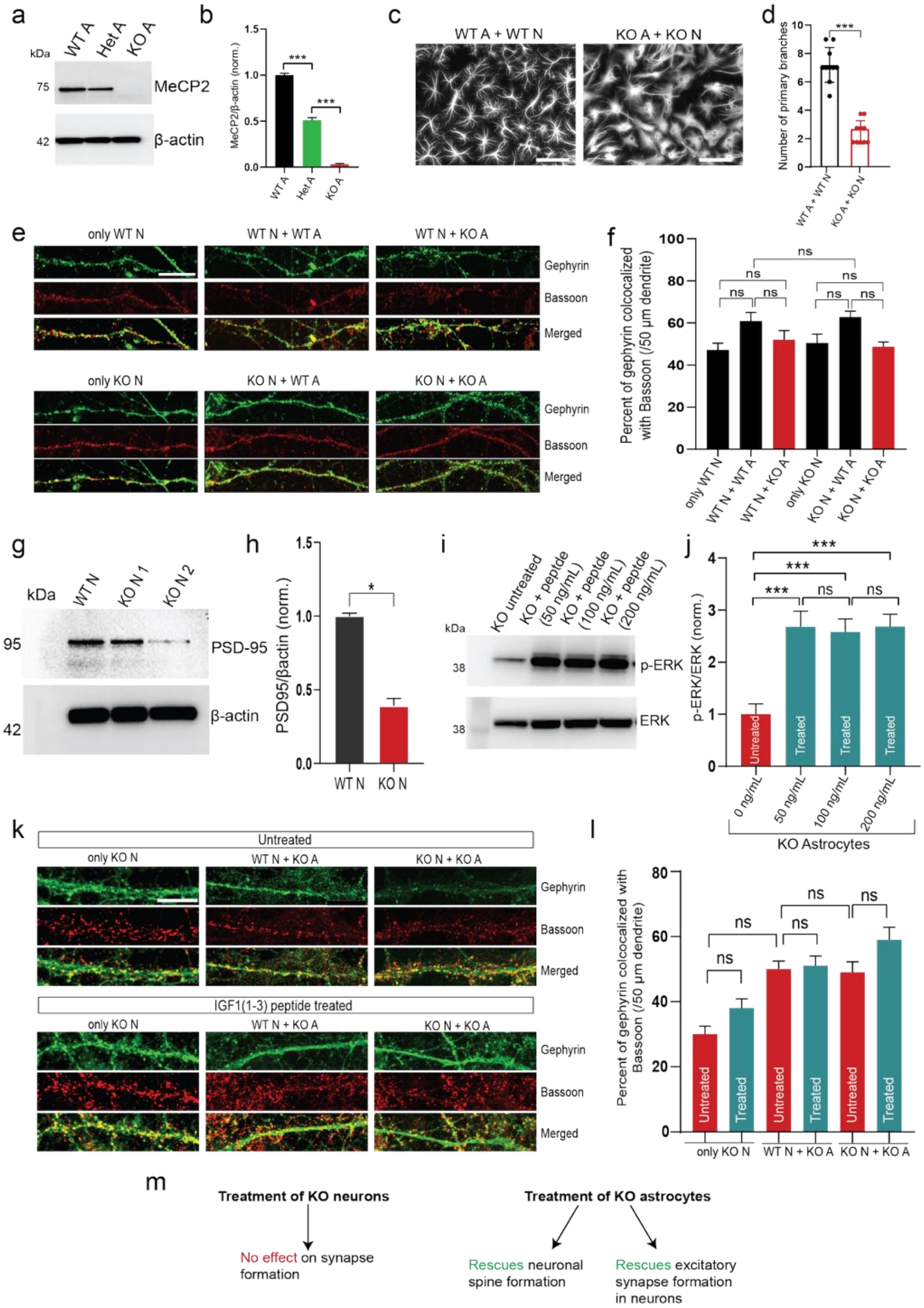

Fig. S1. MeCP2 loss does not affect inhibitory synapse formation. (a-b) Western blot (a) and its quantitation (b) showing MeCP2 protein levels in wild-type (WT), heterozygous (Het) and MeCP2 null astrocytes (KO). ***, $p < 0.001$; one-way ANOVA followed by Tukey's post-hoc test. (c) Representative images of astrocytes stained with GFAP across coculture conditions (scale bar = 250 µm). (d) Quantification of number of primary branches of astrocytes cocultured with neurons. **, $p < 0.01$; ***, $p < 0.05$; ns, non-significant; one way ANOVA followed by Tukey's post-hoc test. (e) Representative images of Bassoon (presynaptic, red) and gephyrin (postsynaptic, green) in dendrites across coculture conditions (scale bar = 10 µm). (f) Quantification of gephyrin/Bassoon colocalization (% per 50 µm dendrite; n = 6 cultures; ns, non-significant). (g-h) Western blot analysis (g) and quantification (h) of PSD-95 levels in neuronal lysates (*$p < 0.05$; one-way ANOVA with Tukey's post hoc test). (i-j) Western blot (i) and its quantitation (j) to analyze dose-dependent p-ERK activation in KO astrocytes treated with IGF1(1-3) peptide (50–200 ng/mL; ***, $p < 0.001$ vs. untreated). All doses were equally effective in elevating p-ERK levels. (k-l) Gephyrin/Bassoon colocalization remains unchanged post-treatment as seen in representative images in (k) and quantitation in (l). ns, non-significant (scale bar = 10 µm). (m) Schematic summarizing the key takeaways from Fig. 1- treatment of neurons alone is unable to rescue excitatory synapse numbers in neurons, however, treatment of astrocytes can rescue both neuronal morphology and neuronal synapse formation.

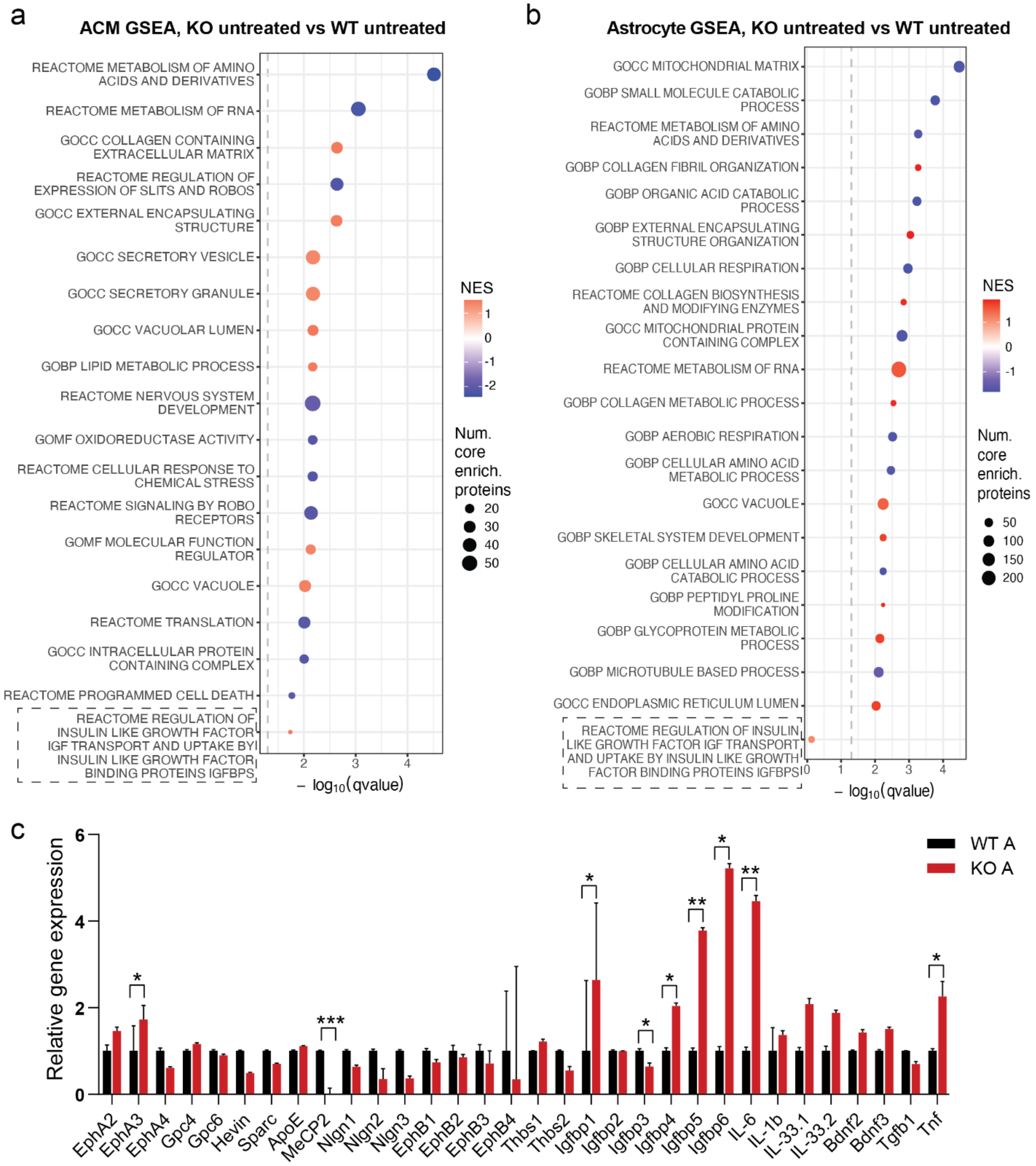

Fig. S2. GSEA of astrocyte-conditioned media (ACM) and whole astrocytes. (a) GSEA of ACM proteins showing activated (red) and suppressed (blue) pathways in KO vs. WT astrocytes. Dotted grey line indicates FDR $q < 0.05$. The significant IGFBP related pathway is highlighted. (b) Astrocyte GSEA highlighting activated (red) and suppressed (blue) pathways in KO vs. WT astrocytes pathways. Dotted grey line indicates FDR $q < 0.05$. (c) qPCR validation of dysregulated genes in KO versus WT astrocytes confirms proteomic findings: Significant upregulation of IGFBPs including IGFBP1, IGFBP4, IGFBP5, IGFBP6, and synaptogenic factors, EphA3 and Tnf. (n = 3 biological replicates; ANOVA with Tukey's post-hoc). Note that unlike its protein levels, IGFBP2 mRNA levels are not high suggesting post-translational regulation.

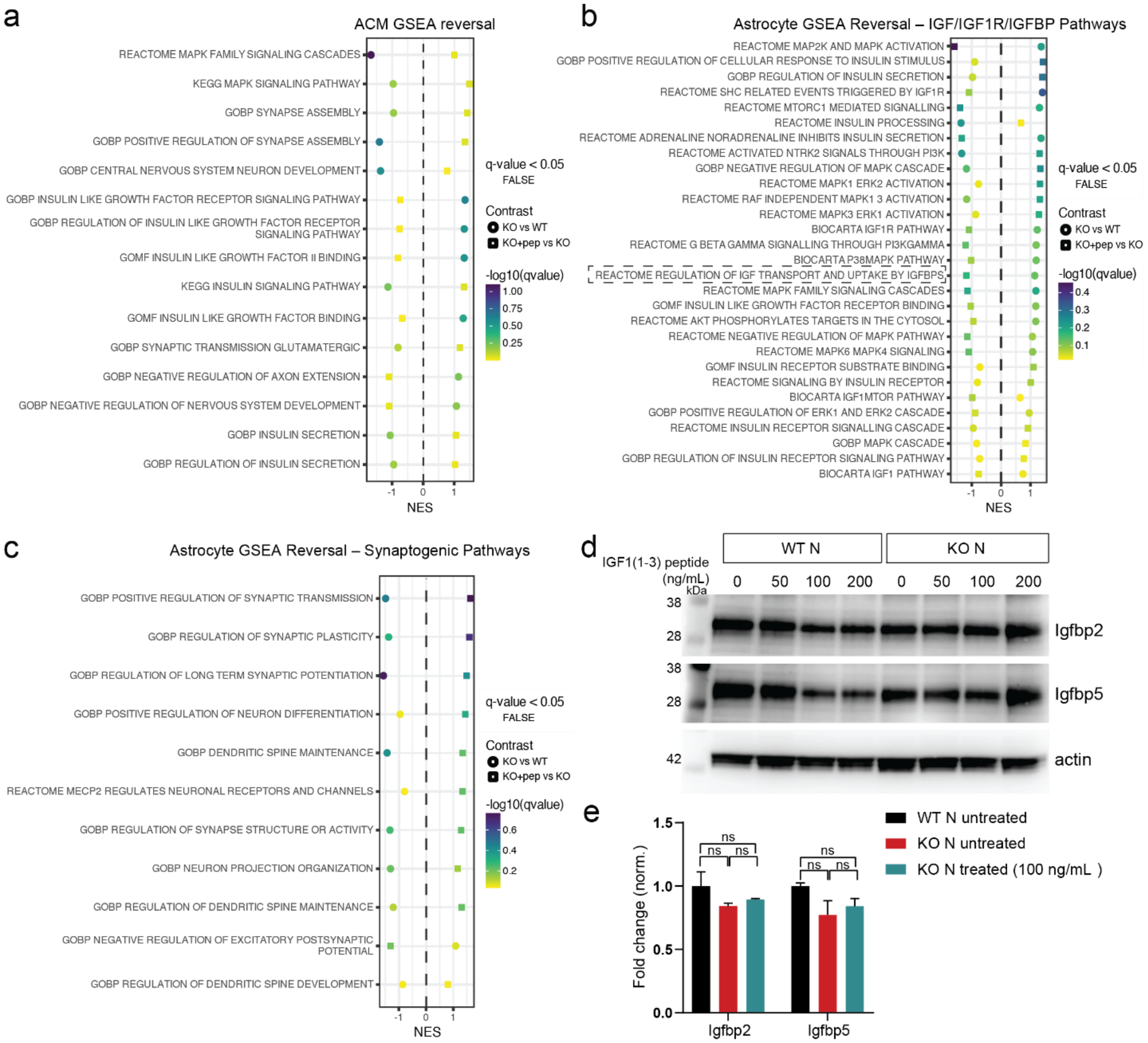

Fig. S3. Treatment with the peptide reverses neuronal and IGF signaling related pathways in astrocytes. (a) GSEA NES plot showing reversal of selected pathways associated with neuronal synaptogenesis and IGF1 signaling in treated vs. untreated KO ACM. Pathways were selected based on relevance to synaptic development and IGF1-dependent signaling. X-axis shows the normalized enrichment score (NES); all the pathways shown here are suppressed in untreated KO ACM and are activated upon peptide treatment (q > 0.05). (b, c) GSEA NES plot showing reversal of selected pathways in astrocytes. IGF1-related pathways are shown in panel (b) and neuronal synaptogenesis-related pathways are shown in panel (c). Note the reversal of pathways related to IGF1R activation and IGFBPs in (b). (d) Western blot analysis of IGFBP2 and IGFBP5 levels in wild-type (WT) and knockout (KO) neurons, demonstrating no detectable changes in neuronal IGFBP expression. (e) Quantification of IGFBP2 and IGFBP5 protein levels from three independent experiments shown in panel (d). Data are presented as mean ± SEM. ns, not significant.

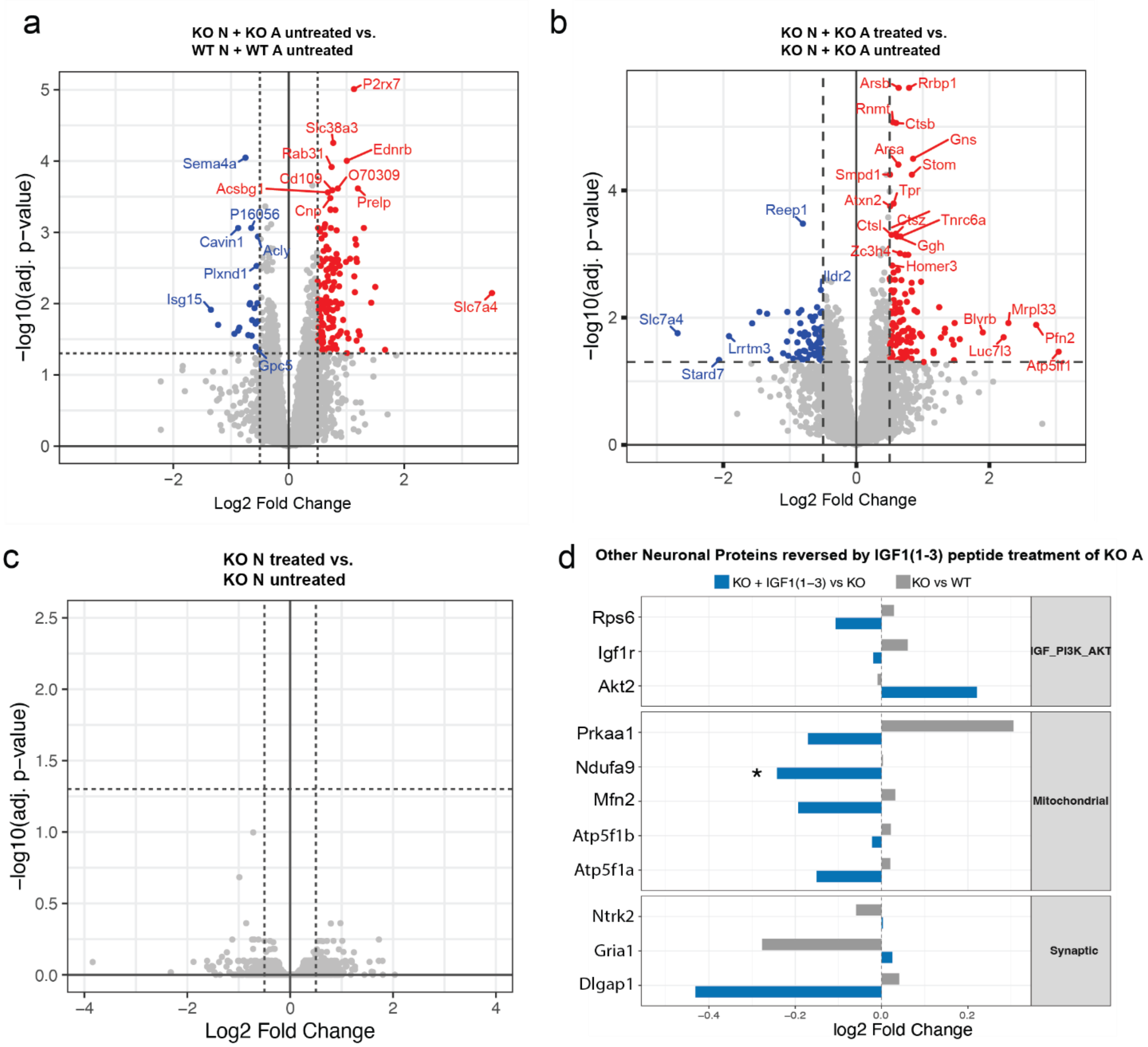

Fig. S4. Peptide-treated astrocytes rescue neuronal synaptic and signaling pathways. (a) Volcano plot showing DEPs in neurons from untreated KO N + KO A vs. WT N + WT A co-cultures. (b) Volcano plot showing DEPs in neurons from KO N + KO A treated vs. untreated co-cultures. Synaptic proteins such as Homer3 are upregulated. Note the clear reversal of Slc7a4 (an amino acid transporter) in b. (c) Volcano plot showing no significant DEPs in treated vs. untreated KO neurons. (d) Reversal of some other proteins of interest in KO neurons after co-culture with treated KO A, based on their log2 fold change. * FDR < 0.05.

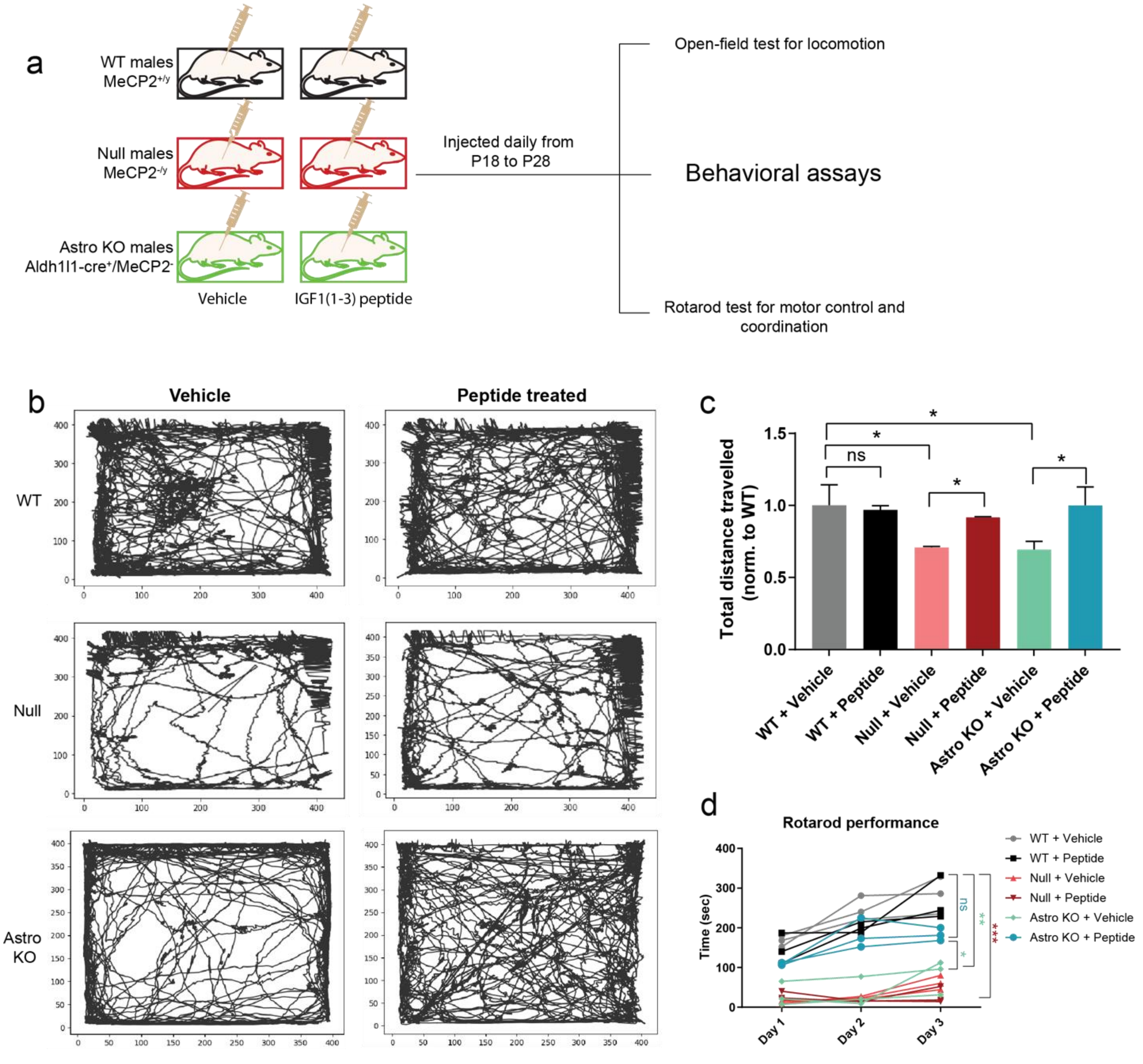

Fig. S5. Behavioral rescue in MeCP2 KO mice by IGF1(1-3) peptide. (a) Experimental timeline: daily peptide injections (0.02 mg/g) (P18–P28) in WT, null ($MeCP2^{-/y}$), and astrocyte-specific KO ($Aldh1l1\text{-}cre^{+}/MeCP2^{-}$) males followed by open-field and rotarod tests. (b-c) Open-field trajectories (b) and total distance traveled (normalized to WT + vehicle) (c) are reduced in both null KO and astrocyte-specific KO and peptide treatment rescues locomotion in both groups of animals. (*, $p < 0.05$ for null/astro KO + peptide vs. WT + vehicle). (d) Rotarod performance is impaired in both KO groups; peptide improves latency to fall in astrocyte-specific KO but not in null mice (*$p < 0.05$; **$p < 0.01$; ***$p < 0.05$; ns, non-significant; one-way ANOVA with Tukey's post hoc). N = 3 mice per group.

Supplementary Tables

Table S1: Differential protein expression analyses for ACM KO untreated vs. WT untreated and KO+peptide vs. KO untreated comparisons

Table S2: Differential protein expression analyses for whole cell astrocytes KO untreated vs. WT untreated and KO+peptide vs. KO untreated comparisons

Table S3: GSEA results for ACM KO untreated vs. WT untreated differential proteomics analysis

Table S4: GSEA results for whole cell astrocytes KO untreated vs. WT untreated differential proteomics analysis

Table S5: Combined GSEA results for ACM- KO+peptide vs. KO untreated and KO untreated vs. WT untreated differential proteomics analysis sorted by absolute NES sum

Table S6: Combined GSEA results for whole cell astrocytes- KO+peptide vs. KO untreated and KO untreated vs. WT untreated differential proteomics analysis sorted by absolute NES sum

Table S7: Overrepresentation of GO terms in biotinylated IGF1(1-3)-associated proteins in WT and KO astrocytes

Table S8: Differential protein expression analyses for KO N + KO A untreated vs. WT N + WT A untreated and KO N + KO A+peptide vs. KO N + KO A untreated comparisons

Table S9: Combined GSEA results for neurons- KO N + KO A+peptide vs. KO N + KO A untreated and KO N + KO A untreated vs. WT N + WT A untreated differential proteomics analysis sorted by absolute NES sum